A search for sparticles in zero lepton final states

Russell W. Smith

Submitted in partial fulfillment of the
requirements for the degree of
Doctor of Philosophy
in the Graduate School of Arts and Sciences

COLUMBIA UNIVERSITY

2016

ABSTRACT

A search for sparticles in zero lepton final states

Russell W. Smith

TODO : Here's where your abstract will eventually go. The above text is all in the center, but the abstract itself should be written as a regular paragraph on the page, and it should not have indentation. Just replace this text.

Contents

Acknowledgements

Dedication

Chapter 1

Introduction

Particle physics is a remarkably successful field of scientific inquiry. The ability to precisely predict the properties of a exceedingly wide range of physical phenomena, such as the description of the cosmic microwave background [1, 2], the understanding of the anomalous magnetic dipole moment of the electron [3, 4], and the measurement of the number of weakly-interacting neutrino flavors [5] is truly amazing.

The theory that has allowed this range of predictions is the *Standard Model* of particle physics (SM). The Standard Model combines the electroweak theory of Glashow, Weinberg, and Salam [6–8] with the theory of the strong interactions, as first envisioned by Gell-Mann and Zweig [9, 10]. This quantum field theory (QFT) contains a tiny number of particles, whose interactions describe phenomena up to at least the TeV scale. These particles are manifestations of the fields of the Standard Model, after application of the Higgs Mechanism. The particle content of the SM consists only of the six quarks, the six leptons, the four gauge bosons, and the scalar Higgs boson.

Despite its impressive range of described phenomena, the Standard Model has some theoretical and experimental deficiencies. The SM contains 26 free parameters [1]. It would be more theoretically pleasing to understand these free parameters in terms of a more fundamental theory. The major theoretical concern of the Standard Model, as it pertains to this thesis, is the *hierachy problem*[11–15]. The light mass

[1] This is the Standard Model corrected to include neutrino masses. These parameters are the fermion masses (6 leptons, 6 quarks), CKM and PMNS mixing angles (8 angles, 2 CP-violating phases), W/Z/Higgs masses (3), the Higgs field expectation value, and the couplings of the strong, weak, and electromagnetic forces (3 α_{force}) .

of the Higgs boson (125 GeV) should be quadratically dependent on the scale of UV physics, due to the quantum corrections from high-energy physics processes. The most perplexing experimental issue is the existence of *dark matter*, as demonstrated by galactic rotation curves [16–22]. This data has shown that there exists additional matter which has not yet been seen interacting with the particles of the Standard Model. There is no particle in the SM which can act as a candidate for dark matter.

Both of these major issues, as well as numerous others, can be solved by the introduction of *supersymmetry* (SUSY) [15, 23–35]. In supersymmetric theories, each SM particles has a so-called *superpartner*, or sparticle partner, differing from given SM particle by 1/2 in spin. These theories solve the hierachy problem, since the quantum corrections induced from the superpartners exactly cancel those induced by the SM particles. In addition, these theories are usually constructed assuming $R-$parity, which can be thought of as the "charge" of supersymmetry, with SM particles having $R = 1$ and sparticles having $R = -1$. In collider experiments, since the incoming SM particles have total $R = 1$, the resulting sparticles are produced in pairs. This produces a rich phenomenology, which is characterized by significant hadronic activity and large missing transverse energy ($E_{\mathrm{T}}^{\mathrm{miss}}$), which provide significant discrimination against SM backgrounds [36].

Despite the power of searches for supersymmetry where $E_{\mathrm{T}}^{\mathrm{miss}}$ is a primary discriminating variable, there has been significant interest in the use of other variables to discriminate against SM backgrounds. These include searches employing variables such as αT, $M_{T,2}$, and the razor variables (M_R, R^2) [37–47]. In this thesis, we will present the first search for supersymmetry using the novel Recursive Jigsaw Reconstruction (RJR) technique. RJR can be considered the conceptual successor of the razor variables. We impose a particular final state "decay tree" on an events, which roughly corresponds to a simplified Feynmann diagram in decays containing weakly-interacting particles. We account for the missing degrees of freedom associated to the weakly-interacting particles by a series of simplifying assumptions, which allow us to calculate our variables of interest at each step in the decay tree. This allows an unprecedented understanding of the internal structure of the decay and the ability to construct additional variables to reject Standard Model backgrounds.

This thesis details a search for the superpartners of the gluon and quarks, the gluino and squarks, in final states with zero leptons, with 13.3 fb^{-1}of data using the ATLAS detector. We organzie the thesis as follows. The theoretical foundations of the Standard Model and supersymmetry are described in Chapters 2 and 3. The Large Hadron Collider and the ATLAS detector are presented in Chapters 4 and 5. Chapter 5 provides a detailed description of Recursive Jigsaw Reconstruction and a description of the variables used for the particular search presented in this thesis. Chapter 6 presents the details of the analysis, including details of the dataset, object reconstruction, and selections used. In Chapter 7, the final results are presented; since there is no evidence of a supersymmetric signal in the analysis, we present the final exclusion curves in simplified supersymmetric models.

Chapter 2

The Standard Model

2.1 Overview

A Standard Model is another name for a theory of the internal symmetry group $SU(3)_C \otimes SU(2)_L \otimes U(1)_Y$, with its associated set of parameters. *The* Standard Model refers specifically to a Standard Model with the proper parameters to describe the universe. The SM is the culmination of years of work in both theoretical and experimental particle physics. In this thesis, we take the view that theorists cite construct a model with the field content and symmetries as inputs, and write down the most general Lagrangian consistent with those symmetries. Assuming this model is compatible with nature (in particular, the predictions of the model are consistent with previous experiments), experimentalists are responsible measuring the parameters of this model This will be applicable for this chapter and the following one.

Additional theoretical background is in 10.6. The philosophy and notations are inspired by [48, 49].

2.2 Field Content

The Standard Model field content is

$$\begin{aligned} \text{Fermions } &: Q_L(3,2)_{+1/3}, U_R(3,1)_{+4/3}, D_R(3,1)_{-2/3}, L_L(1,2)_{-1}, E_R(1,1)_{-2} \\ \text{Scalar (Higgs) } &: \phi(1,2)_{+1} \qquad (2.1) \\ \text{Vector Fields } &: G^\mu(8,1)_0, W^\mu(1,3)_0, B^\mu(1,1)_0 \end{aligned}$$

where the $(A, B)_Y$ notation represents the irreducible representation under $SU(3)$ and $SU(2)$, with Y being the electroweak hypercharge. Each of these fermion fields has an additional index, representing the three generation of fermions.

We observed that Q_L, U_R, and D_R are triplets under $SU(3)_C$; these are the *quark* fields. The *color* group, $SU(3)_C$ is mediated by the *gluon* field $G^\mu(8,1)_0$, which has 8 degrees of freedom. The fermion fields $L_L(1,2)_{-1}$ and $E_R(1,1)_{-2}$ are singlets under $SU(3)_C$; we call them the *lepton* fields.

Next, we note the "left-handed" ("right-handed") fermion fields, denoted by L (R) subscript, The left-handed fields form doublets under $SU(2)_L$. These are mediated by the three degrees of freedom of the "W" fields $W^\mu(1,3)_0$. These fields only act on the left-handed particles of the Standard Model. This is the reflection of the "chirality" of the Standard Model; the left-handed and right-handed particles are treated differently by the electroweak forces. The right-handed fields, U_R, D_R, and E_R, are singlets under $SU(2)_L$.

The $U(1)_Y$ symmetry is associated to the $B^\mu(1,1)_0$ boson with one degree of freedom. The charge Y is known as the electroweak hypercharge.

To better understand the phenomenology of the Standard Model, let us investigate each of the *sectors* of the Standard Model separately.

Electroweak sector

The electroweak sector refers to the $SU(2)_L \otimes U(1)_Y$ portion of the Standard Model gauge group. Following our philosophy of writing all gauge-invariant and renormalizable terms, the electroweak Lagrangian can be written as

$$\mathcal{L} = W_a^{\mu\nu} W_{\mu\nu}^a + B^{\mu\nu} B_{\mu\nu} + (D^\mu \phi)^\dagger D_\mu \phi - \mu^2 \phi^\dagger \phi - \lambda(\phi^\dagger \phi)^2. \tag{2.2}$$

where $W_a^{\mu\nu}$ are the three ($a = 1, 2, 3$) gauge bosons associated to the $SU(2)_L$ gauge group, $B^{\mu\nu}$ is the one gauge boson of the $U(1)_Y$ gauge group, and ϕ is the complex

Figure 2.1: Sombrero potential

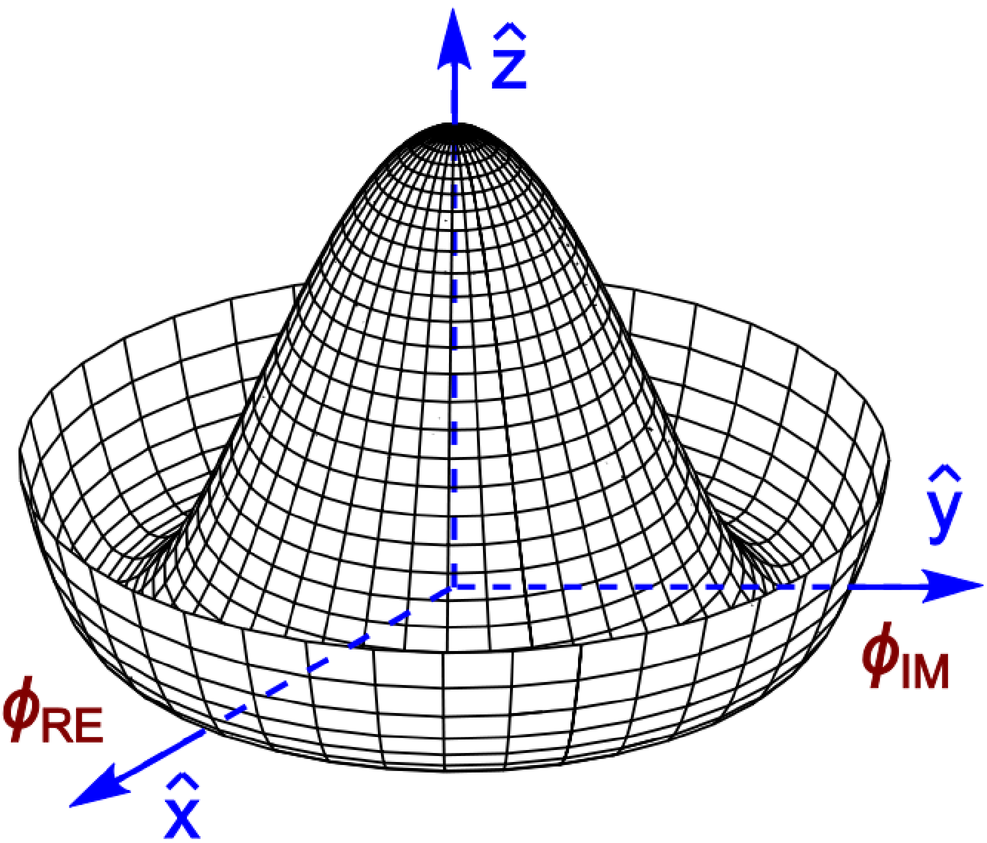

Higgs multiplet. The covariant derivative D^μ is given by

$$D^\mu = \partial^\mu + \frac{ig}{2} W_a^\mu \sigma_a + \frac{ig'}{2} B^\mu \tag{2.3}$$

where $i\sigma_a$ are the Pauli matrices times the imaginary constant, which are the generators for $SU(2)_L$, and g and g' are the $SU(2)_L$ and $U(1)_Y$ coupling constants, respectively. The field strength tensors $W_a^{\mu\nu}$ and $B^{\mu\nu}$ are given by the commutator of the covariant derivative associated to each field

$$\begin{aligned} B^{\mu\nu} &= \partial^\mu B^\nu - \partial^\nu B^\mu \\ W_a^{\mu\nu} &= \partial^\mu W_a^\nu - \partial^\nu W_a^\mu - g\epsilon_{abc} W_a^\mu W_b^\nu, \qquad\qquad i = 1, 2, 3 \end{aligned} \tag{2.4}$$

170

The terms in the Lagrangian 2.2 proportional to μ^2 and λ make up the "Higgs potential" [50]. As normal (see Appendix 10.6), we restrict $\lambda > 0$ to guarantee our potential is bounded from below, and we also require $\mu^2 < 0$, which gives us the standard "sombrero" potential shown in 2.1.

This potential has infinitely many minima at $<\phi>= \sqrt{2m/\lambda}$; the ground state is *spontaneously* broken by the choice of ground state, which induces a vacuum expection value (VEV). Without loss of generality, we can choose the Higgs field ϕ to point in the real direction, and write the Higgs field ϕ in the following form :

$$\phi = \frac{1}{\sqrt{2}} \exp(\frac{i}{v}\sigma_a\theta_a) \begin{pmatrix} 0 \\ v + h(x) \end{pmatrix}. \tag{2.5}$$

We choose a gauge to rotate away the dependence on θ_a, such that we can write simply

$$\phi = \frac{1}{\sqrt{2}} \begin{pmatrix} 0 \\ v + h(x) \end{pmatrix}. \tag{2.6}$$

Now, we can see how the masses of the vector bosons are generated from the application of the Higgs mechanism. We plug Eq.2.6 back into the electroweak Lagrangian, and only showing the relevant mass terms in the vacuum state where $h(x) = 0$ see that (dropping the Lorentz indices) :

$$\begin{aligned} \mathcal{L}_M &= \frac{1}{8} \left| \begin{pmatrix} gW_3 + g'B & g(W_1 - iW_2) \\ g(W_1 + iW_2) & -gW_3 + g'B \end{pmatrix} \begin{pmatrix} 0 \\ v \end{pmatrix} \right|^2 \\ &= \frac{g^2v^2}{8} \left[W_1^2 + W_2^2 + (\tfrac{g'}{g}B - W_3)^2 \right] \end{aligned} \tag{2.7}$$

Defining the *Weinberg* angle $\tan(\theta_W) = g'/g$ and the following *physical* fields :

$$\begin{aligned} W^{\pm} &= \frac{1}{\sqrt{2}}(W_1 \mp iW_2) \\ Z^0 &= \cos\theta_W W_3 - \sin\theta_W B \\ A^0 &= \sin\theta_W W_3 + \cos\theta_W B \end{aligned} \tag{2.8}$$

we can write the piece of the Lagrangian associated to the vector boson masses as

$$\mathcal{L}_{M_V} = \frac{1}{4}g^2v^2W^+W^- + \frac{1}{8}(g^2 + g'^2)v^2Z^0Z^0. \tag{2.9}$$

and we have the following values of the masses for the vector bosons :

$$\begin{aligned} m_W^2 &= \frac{1}{4}v^2g^2 \\ m_Z^2 &= \frac{1}{4}v^2(g^2 + g'^2) \\ m_A^2 &= 0 \end{aligned} \tag{2.10}$$

We thus see how the Higgs mechnanism gives rise to the masses of the $W^\pm$ and Z boson in the Standard Model; the mass of the photon is zero, as expected. The $SU(2)_L \otimes U(1)_Y$ symmetry of the initially massless $W_{1,2,3}$ and B fields is broken to the $U(1)_{EM}$. Of the four degrees of freedom in the complex Higgs doublet, three are "eaten" when we give mass to the $W^\pm$ and Z_0, while the other degree of freedom is the Higgs particle, as found in 2012 by the ATLAS and CMS collaborations [51, 52].

Quantum Chromodynamics

Quantum chromodynamics (or the theory of the *strong* force) characterizes the behavior of *colored* particles, collectively known as *partons*. The partons of the Standard Model are the (fermionic) quarks, and the (bosonic) gluons. The strong force is governed by $SU(3)_C$, an unbroken symmetry in the Standard Model, which implies the gluon remains massless. Defining the covariant derivative for QCD as

$$D^\mu = \partial^\mu + ig_sG_a^\mu L_a, a = 1, ..., 8 \tag{2.11}$$

where L_a are the generators of $SU(3)_C$, and g_s is the coupling constant of the strong force. The QCD Lagrangian then is given by

$$\mathcal{L}_{\text{QCD}} = i\bar{\psi}_f D_\mu \gamma^\mu \psi_f - \frac{1}{4}G_{a,\mu\nu}G_a^{\mu\nu} \tag{2.12}$$

where the summation over f is for quarks *families*, and $G_a^{\mu\nu}$ is the gluon field strength tensor, given by

$$G_a^{\mu\nu} = \partial^\mu G_a^\nu - \partial^\nu G_a^\mu - g_s f^{abc} G_b^\mu G_c^\nu, a, b, c = 1, ..., 8 \tag{2.13}$$

where f^{abc} are the structure constants of $SU(3)_C$, which are analogous to ϵ_{abc} for $SU(2)_L$. The kinetic term for the quarks is contained in the standard ∂_μ term, while the field strength term contains the interactions between the quarks and gluons, as well as the gluon self-interactions.

Written down in this simple form, the QCD Lagrangian does not seem much different from the QED Lagrangian, with the proper adjustments for the different group structures. The gluon is massless, like the photon, so one could näively expect an infinite range force, and it pays to understand why this is not the case. The reason for this fundamental difference is the gluon self-interactions arising in the field strength tensor term of the Lagrangian. This leads to the phenomena of *color confinement*, which describes how one only observes color-neutral particles alone in nature. In contrast to the electromagnetic force, particles which interact via the strong force experience a *greater* force as the distance between the particles increases. At long distances, the potential is given by $V(r) = -kr$. At some point, it is more energetically favorable to create additional partons out of the vacuum than continue pulling apart the existing partons, and the colored particles undergo *fragmentation*. This leads to *hadronization*. Bare quarks and gluons are actually observed as sprays of hadrons (primarly kaons and pions); these sprays are known as *jets*, which are what are observed by experiments.

It is important to recognize the importance of understanding these QCD interactions in high-energy hadron colliders such as the LHC. Since protons are hadrons, proton-proton collisions such as those produced by the LHC are primarily governed by the processes of QCD. In particular, by far the most frequent process observed in LHC experiments is dijet production from gluon-gluon interactions (see Fig.2.2). These

Figure 2.2: Cross-sections of various Standard Model processes

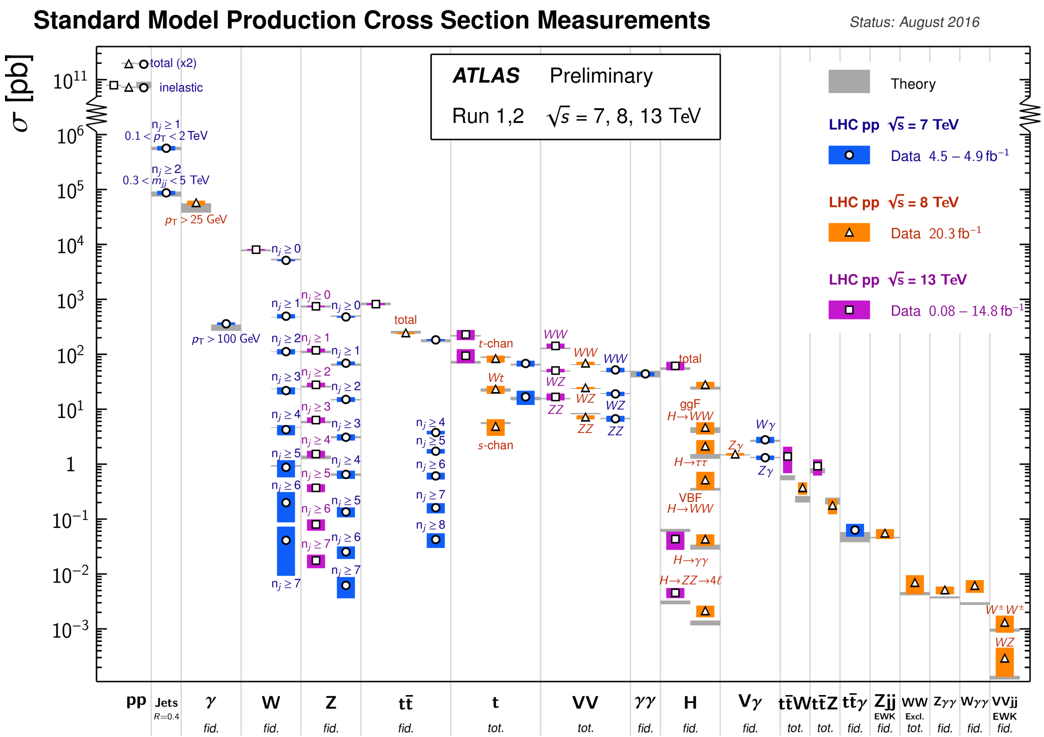

gluons that interact are part of the *sea* particles inside the proton; the simple $p = uud$ model does not apply. The main *valence uud* quarks are constantly interacting via gluons, which can themselves radiate gluons or split into quarks, and so on. A more useful understanding is given by the colloquially-known *bag* model [53, 54], where the proton is seen as a "bag" of (in principle) infinitely many partons, each with energy $E < \sqrt{s} = 6.5$ TeV. One then collides this (proton) bag with another, and views the products of this very complicated collision, where calculations include many loops in nonpertubative QCD calculations.

Fortunately, we are generally saved by the QCD factorization theorems [55]. This allows one to understand the hard (i.e. short distance or high energy) $2 \rightarrow 2$ parton process using the tools of perturbative QCD, while making series of approximations known as a *parton shower* model to understand the additional corrections from nonpertubative QCD. We will discuss the reconstruction of jets by experiments in Ch.5.

Fermions

We will now look more closely at the fermions in the Standard Model [56].

As noted earlier in Sec.2.2, the fermions of the Standard Model can be first distinguished between those that interact via the strong force (quarks) and those which do not (leptons).

There are six leptons in the Standard Model, which can be placed into three *generations*.

$$\begin{pmatrix} e \\ \nu_e \end{pmatrix}, \begin{pmatrix} \mu \\ \nu_\mu \end{pmatrix}, \begin{pmatrix} \tau \\ \nu_\tau \end{pmatrix} \tag{2.14}$$

There is the electron (e), muon (μ), and tau (τ), each of which has an associated neutrino (ν_e, ν_μ, ν_τ). Each of the so-called charged ("electron-like") leptons has electromagnetic charge -1, while the neutrinos all have $q_{EM} = 0$.

Often in an experimental context, lepton is used to denote the stable electron and metastable muon, due to their striking experimental signatures. Taus are often treated separately, due to their much shorter lifetime of $\tau_\tau \sim 10^{-13}s$; these decay through hadrons or the other leptons, so often physics analyses at the LHC treat them as jets or leptons, as will be done in this thesis.

As the neutrinos are electrically neutral, nearly massless, and only interact via the weak force, it is quite difficult to observe them directly. Since LHC experiments rely overwhelmingly on electromagnetic interactions to observe particles, the presence of neutrinos is not observed directly. Neutrinos are instead observed by the conservation of four-momentum in the plane transverse to the proton-proton collisions, known as *missing transverse energy*.

There are six quarks in the Standard Model : up, down, charm, strange, top, and bottom. Quarks are similar organized into three generations :

$$\begin{pmatrix} u \\ d \end{pmatrix}, \begin{pmatrix} c \\ s \end{pmatrix}, \begin{pmatrix} t \\ b \end{pmatrix} \tag{2.15}$$

where we speak of “up-like” quarks and “down-like” quarks.

Each up-like quark has charge $q_{up} = 2/3$, while the down-like quarks have $q_{down} = -1/3$. At the high energies of the LHC, one often makes the distinction between the light quarks (u, d, c, s), the bottom quark, and top quark. In general, due to the hadronization process described above, the light quarks, with masses $m_q <\sim 1.5 GeV$ are indistinguishable by LHC experiments. Their hadronic decay products generally have long lifetimes and they are reconstructed as jets.[1]. The bottom quark hadronizes primarily through the B-mesons, which generally travels a short distance before decaying to other hadrons. This allows one to distinguish decays via $b-$quarks form other jets; this procedure is known as *b-tagging* and will be discussed more in Ch.5. Due to its large mass, the top quark decays before it can hadronize; there are no bound states associated to the top quark. The top is of particular interest at the LHC; it has a striking signature through its most common decay mode $t \rightarrow Wb$. Decays via tops, especially $t\bar{t}$ are frequently an important signal decay mode, or an important background process.

Interactions in the Standard Model

We briefly overview the entirety of the fundamental interactions of the Standard Model; these can also be found in 2.3.

The electromagnetic force, mediated by the photon, interacts with via a three-point coupling all charged particles in the Standard Model. The photon thus interacts with all the quarks, the charged leptons, and the charged $W^{\pm}$ bosons.

The weak force is mediated by three particles : the $W^{\pm}$ and the Z^0. The Z^0 can interacts with all fermions via a three-point coupling. A real Z_0 can thus decay to a fermion-antifermion pair of all SM fermions except the top quark, due to its large

[1]In some contexts, charm quarks are also treated as a separate category, although it is quite difficult to distinguish charm quarks from the other light quarks.

Figure 2.3: The interactions of the Standard Model

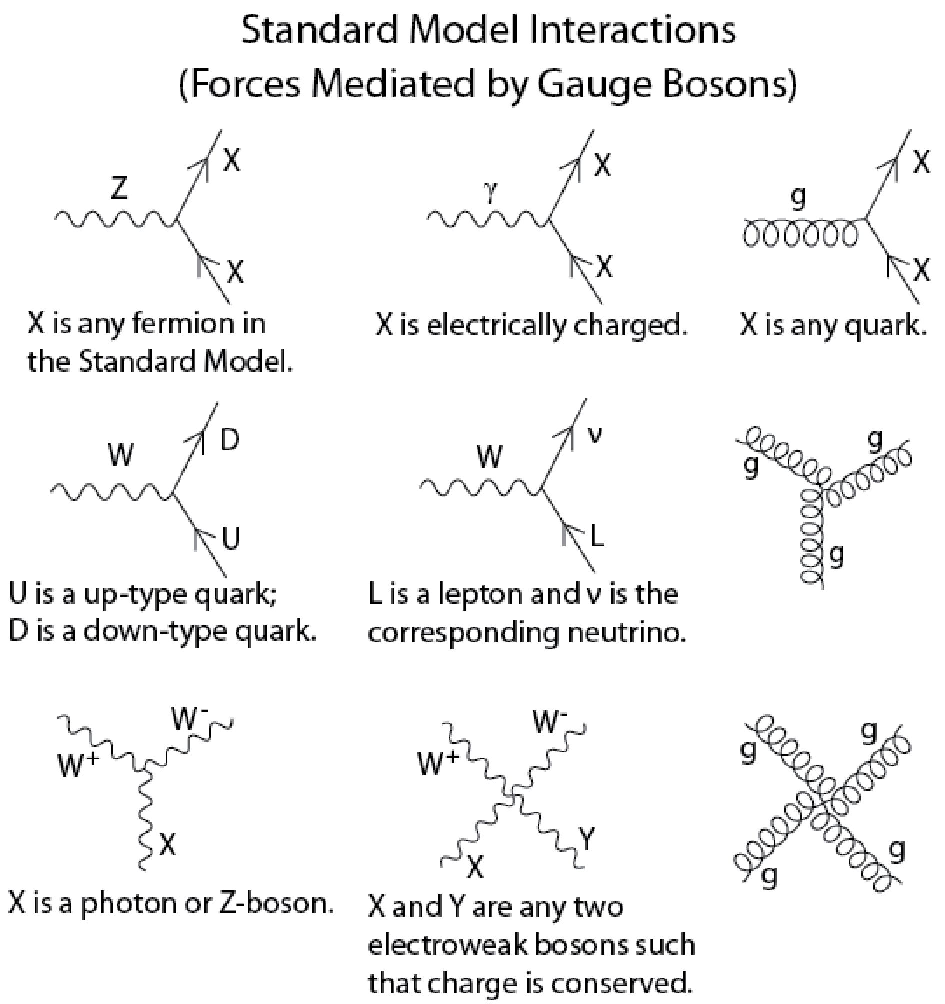

mass. The $W^{\pm}$ has two important three-point interactions with fermions. First, the $W^{\pm}$ can interact with an up-like quark and a down-like quark; an important example in LHC experiments is $t \to Wb$ The coupling constants for these interactions are encoded in the unitary matrix known as the Cabibbo–Kobayashi–Maskawa (CKM) matrix [57, 58], and are generally known as flavor-changing interactions. Secondly, the $W^{\pm}$ interacts with a charged lepton and its corresponding neutrino. In this case, the unitary matrix that corresponds to CKM matrix for quarks is the identity matrix, which forbids (fundamental) vertices such as $\mu \to We$. For leptons, instead this is a two-step process : $\mu \to \nu_m uW \to \nu_m u\bar{\nu}_e e$. Finally, there are the self-interactions of the weak gauge bosons. There is a three-point and four-point interaction; all combinations are allowed which conserve electric charge.

The strong force is mediated by the gluon, which as discussed above also carries the strong color charge. There is the fundamental three-point interaction, where a quark radiates a gluon. Additionally, there are the three-point and four-point gluon-only interactions.

2.3 Deficiencies of the Standard Model

At this point, it is quite easy to simply rest on our laurels. This relatively simple theory is capable of explaining a very wide range of phenomenom, which ultimately break down only to combinations of nine diagrams shown in Fig.2.3. Unfortunately, there are some unexplained problems with the Standard Model. We cannot go through all of the potential issues in this thesis, but we will motivate the primary issues which naturally lead one to *supersymmetry*, as we will see in Ch.3.

The Standard Model has many free paramaters; see Table 2.1 In general, we prefer models with less free parameters. A great example of this fact, and the primary experimental evidence for EWSB, is the relationship between the couplings of the weak force and the masses of the gauge bosons of the weak force :

$$\rho \equiv \frac{m_W^2}{m_Z^2 \cos^2\theta_W} \stackrel{?}{=} 1 \tag{2.16}$$

where ? indicates that this is a testable prediction of the Standard Model (in particular, that the gauge bosons gain mass through EWSB). This relationship has been measured within experimental and theoretical predictions. We would like to produce additional such relationships, which would exist if the Standard Model is a low-energy approximation of some other theory.

An additional issue is the lack of *gauge coupling unification*. The couplings of any quantum field theory "run" as a function of the distance scales (or inversely,

Table 2.1: Parameters of the Standard Model. For values dependent on the renormalization scheme, we use a combination of the on-shell normalization scheme [59–62] and modified minimal subtraction scheme with $m_{\bar{M}S}$ as indicated in the table[63]

m_e	Electron mass	511 keV
m_μ	Muon mass	105.7 MeV
m_τ	Tau mass	1.78 GeV
m_u	Up quark mass	1.9 MeV ($m_{\bar{M}S} = 2GeV$)
m_d	Down quark mass	4.4 MeV ($m_{\bar{M}S} = 2GeV$)
m_s	Strange quark mass	87 MeV ($m_{\bar{M}S} = 2GeV$)
m_c	Charm quark mass	1.32 GeV ($m_{\bar{M}S} = m_c$)
m_b	Bottom quark mass	4.24 GeV ($m_{\bar{M}S} = m_b$)
m_t	Top quark mass	172.7 GeV (on-shell renormalization)
θ_{12} CKM	12-mixing angle	13.1°
θ_{23} CKM	23-mixing angle	2.4°
θ_{13} CKM	13-mixing angle	0.2°
δ CKM	CP-violating Phase	0.995
g'	U(1) gauge coupling	0.357 ($m_{\bar{M}S} = m_Z$)
g	SU(2) gauge coupling	0.652 ($m_{\bar{M}S} = m_Z$)
g_s	SU(3) gauge coupling	1.221 ($m_{\bar{M}S} = m_Z$)
θQCD	QCD vacuum angle	∼0
VEV	Higgs vacuum expectation value	246 GeV
m_H	Higgs mass	125 GeV

energy scales) of the theory. The idea is closely related to the unification of the electromagnetic and weak forces at the so-called *electroweak scale* of $O(100\text{ GeV})$. One would hope this behavior was repeated between the electroweak forces and the strong force at some suitable energy scale. The Standard Model does automatically not exhibit this behavior, as we can see in Fig.2.4.

The most significant problem with the Standard Model is the *hierarchy problem*. In its most straightforward incarnation, the Higgs scalar field is subject to quantum corrections through loop diagrams, as shown in Fig.2.5. For demonstration, we use the contributions from the top quark, since the top quark has the largest Higgs Yukawa coupling due to its large mass. In general, we should expect these corrections to quadratically dependent on the scale of the ultraviolet physics, Λ. Briefly assume there is no new physics before the Planck scale of gravity, $\Lambda_{\text{Planck}} = 10^{19}$ GeV. In this

Figure 2.4: The running of Standard Model gauge couplings. The Standard Model couplings do not unify at high energies, which indicates it cannot completely describe nature through the Planck scale.

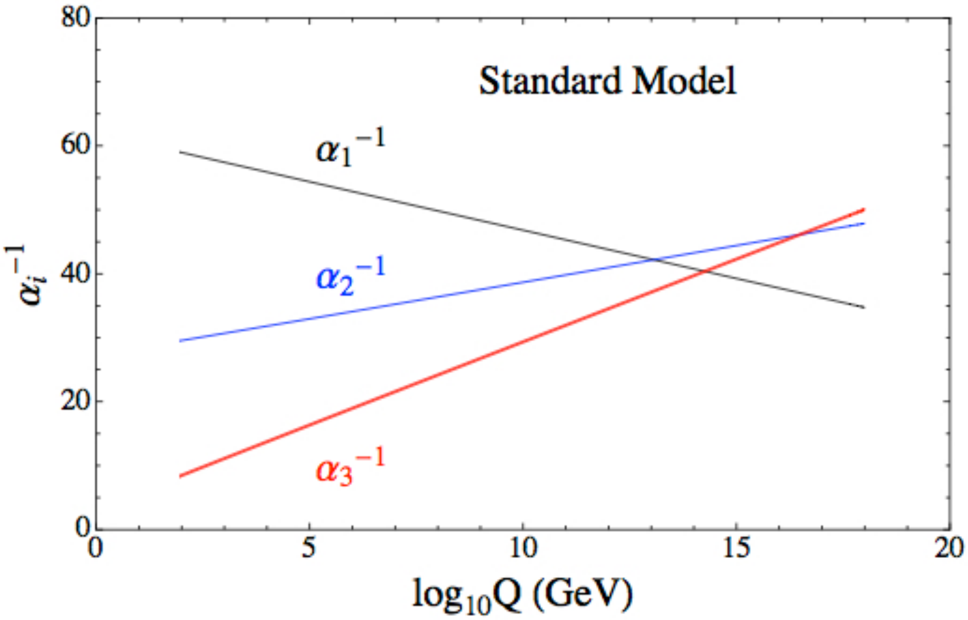

Figure 2.5: The dominant quantum loop correction to the Higgs mass in the Standard Model.

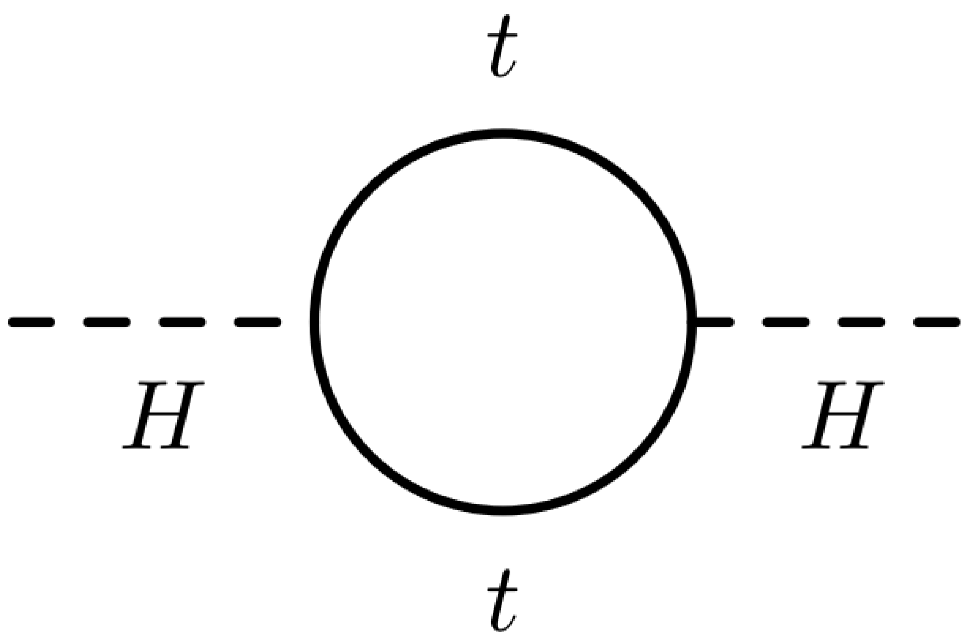

case, we expect the corrections to the Higgs mass like

$$\delta m_H^2 \approx \left(\frac{m_t}{8\pi^2 <\phi>_{VEV}} \right)^2 \Lambda^2_{Planck}. \tag{2.17}$$

To achieve the miraculous cancellation required to get the observed Higgs mass of 125 GeV, one needs to then set the bare Higgs mass m_0, our input to the Standard Model Lagrangian, itself to a *precise* value $\sim 10^{19}$ GeV. This extraordinary level of parameter finetuning is quite undesirable, and within the framework of the Standard Model, there is little that can be done to alleviate this issue.

An additional concern, of a different nature, is the lack of a *dark matter* candidate in the Standard Model. Dark matter was discovered by observing galactic rotation curves, which showed that much of the matter that interacted gravitionally was invisible to our (electromagnetic) telescopes [16–22]. The postulation of the existence of dark matter, which interacts at least through gravity, allows one to understand these galatic rotation curves. Unfortunately, no particle in the Standard Model could possibly be the dark matter particle. The only candidate truly worth another look is the neutrino, but it has been shown that the neutrino content of the universe is simply too small to explain the galatic rotation curves [22, 64]. The experimental evidence from the galactic rotations curves thus show there *must* be additional physics beyond the Standard Model, which is yet to be understood.

In the next chapter, we will see how these problems can be alleviated by the theory of supersymmetry.

Figure 2.6: Particles of the Standard Model

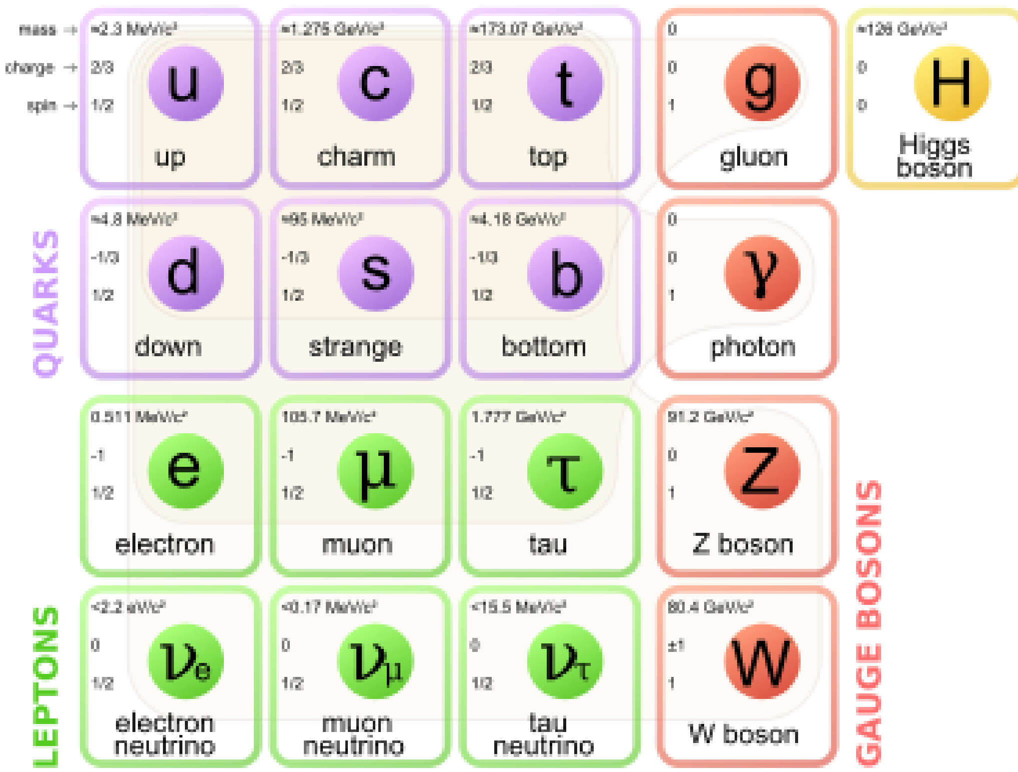

Chapter 3

Supersymmetry

This chapter will introduce supersymmetry (SUSY) [15, 23–35]. We will begin by introducing the concept of a *superspace*, and discuss some general ingredients of supersymmetric theories. This will include a discussion of how the problems with the Standard Model described in Ch.2 are naturally fixed by these theories.

The next step is to discuss the particle content of the *Minimally Supersymmetric Standard Model* (MSSM). As its name implies, this theory contains the minimal additional particle content to make Standard Model supersymmetric. We then discuss the important phenomonological consequences of this theory, especially as it would be observed in experiments at the LHC.

3.1 Supersymmetric theories : from space to superspace

Coleman-Mandula "no-go" theorm

We begin the theoretical motivation for supersymmetry by citing the "no-go" theorem of Coleman and Mandula [65]. This theorem forbids *spin-charge unification*; it states that all quantum field theories which contain nontrivial interactions must be a direct product of the Poincarégroup of Lorentz symmetries, the internal product from of gauge symmetries, and the discrete symmetries of parity, charge conjugation, and time reversal. The assumptions which go into building the Coleman-Mandula theorem are quite restrictive, but there is one unique way out, which has become known as *supersymmetry* [26, 66]. In particular, we must introduce a *spinorial* group generator Q. Alternatively, and equivalently, this can be viewed as the addition of anti-commuting coordinates; space plus these new anti-commuting coordinates is then called *superspace* [67]. We will not investiage this view in detail, but it is also a quite intuitive and beautiful way to construct supersymmetry[15].

Supersymmetry transformations

A *supersymmetric* transformation Q transforms a bosonic state into a fermionic state, and vice versa :

$$Q\,|\text{Fermion}\rangle = |\text{Boson}\rangle \tag{3.1}$$

$$Q\,|\text{Boson}\rangle = |\text{Fermion}\rangle \tag{3.2}$$

To ensure this relation holds, Q must be an anticommuting spinor. Additionally, since spinors are inherently complex, $Q^\dagger$ must also be a generator of the supersymmetry transformation. Since Q and $Q^\dagger$ are spinor objects (with $s = 1/2$), we can see that supersymmetry must be a spacetime symmetry. The Haag-Lopuszanski-Sohnius extension [66] of the Coleman-Mandula theorem [65] is quite restrictive about the forms of such a symmetry. Here, we simply write the (anti-) commutation relations [15] :

$$Q_\alpha, Q^\dagger_{\dot\alpha} = -2\sigma_{\alpha\dot\alpha^\mu} P_\mu \tag{3.3}$$

$$Q_\alpha, Q_{\dot\beta} = Q^\dagger_{\dot\alpha}, Q^\dagger_{\dot\beta} = 0 \tag{3.4}$$

$$[P^\mu, Q_\alpha] = [P^\mu, Q^\dagger_{\dot\alpha}] = 0 \tag{3.5}$$

Supermultiplets

In a supersymmetric theory, we organize single-particle states into irreducible representations of the supersymmetric algebra which are known as *supermultiplets*. Each supermultiplet contains a fermion state $|\mathrm{F}\rangle$ and a boson state $|\mathrm{B}\rangle$; these two states are the known as *superpartners*. These are related by some combination of Q and $Q^\dagger$, up to a spacetime transformation. Q and $Q^\dagger$ commute with the mass-squared operator $-P^2$ and the operators corresponding to the gauge transformations [15]; in particular, the gauge interactions of the Standard Model. In an unbroken supersymmetric theory, this means the states $|\mathrm{F}\rangle$ and $|\mathrm{B}\rangle$ have exactly the same mass, electromagnetic charge, electroweak isospin, and color charges. One can also prove [15] that each supermultiplet contains the exact same number of bosonic (n_B) and fermion (n_F) degrees of freedom. We now explore the possible types of supermultiples one can find in a renormalizable supersymmetric theory.

Since each supermultiplet must contain a fermion state, the simplest type of supermultiplet contains a single Weyl fermion state ($n_F = 2$) which is paired with $n_B = 2$ scalar bosonic degrees of freedom. This is most conveniently constructed as single complex scalar field. We call this construction a *scalar supermultiplet* or *chiral supermultiplet*. The second name is indicative; only chiral supermultiplets can contain fermions whose right-handed and left-handed components transform differently under the gauge interactions (as of course happens in the Standard Model).

The second type of supermultiplet we construct is known as a *gauge* supermultiplet. We take a spin-1 gauge boson (which must be massless due to the gauge symmetry, so $n_B = 2$) and pair this with a single massless Weyl spinor[1]. The gauge bosons transform as the adjoint representation of the their respective gauge groups; their fermionic partners, which are known as gauginos, must also. In particular, the left-handed and right-handed components of the gaugino fermions have the same

[1] Choosing an $s = 3/2$ massless fermion leads to nonrenormalizable interactions.

gauge transformation properties.

Excluding gravity, this is the entire list of supermultiplets which can participate in renormalizable interactions in what is known as $N = 1$ supersymmetry. This means there is only one copy of the supersymmetry generators Q and $Q^\dagger$. This is essentially the only "easy" phenomenological choice, since it is the only choice in four dimensions which allows for the chiral fermions and parity violations built into the Standard Model, and we will not look further into $N > 1$ supersymmtry in this thesis.

The primary goal, after understanding the possible structures of the multiplets above, is to fit the Standard Model particles into a multiplet, and therefore make predictions about their supersymmetric partners. We explore this in the next section.

3.2 Minimally Supersymmetric Standard Model

To construct what is known as the MSSM [**susyPrimer** , 68–71], we need a few ingredients and assumptions. First, we match the Standard Model particles with their corresponding superpartners of the MSSM. We will also introduce the naming of the superpartners (also known as *sparticles*). We discuss a very common additional restraint imposed on the MSSM, known as $R-$parity. We also discuss the concept of soft supersymmetry breaking and how it manifests itself in the MSSM.

Chiral supermultiplets

The first thing we deduce is directly from Sec.**??**. The bosonic superpartners associated to the quarks and leptons *must* be spin 0, since the quarks and leptons must be arranged in a chiral supermultiplet. This is essentially the note above, since the chiral supermultiplet is the only one which can distinguish between the left-handed and right-handed components of the Standard Model particles. The superpartners of the quarks and leptons are known as *squarks* and *sleptons*, or *sfermions* in aggregate.

(for “scalar quarks”, “scalar leptons”, and “scalar fermion”[2]). The “s-” prefix can also be added to the individual quarks i.e. *selectron*, *sneutrino*, and *stop*. The notation is to add a $\sim$ over the corresponding Standard Model particle i.e. $\tilde{e}$, the selectron is the superpartner of the electron. The two-component Weyl spinors of the Standard Model must each have their own (complex scalar) partner i.e. e_L, e_R have two distinct partners : $\tilde{e_L}, \tilde{e_R}$. As noted above, the gauge interactions of any of the sfermions are identical to those of their Standard Model partners.

Due to the scalar nature of the Higgs, it must obviously lie in a chiral supermultiplet. To avoid gauge anomolies and ensure the correct Yukawa couplings to the quarks and leptons[15], we must add additional Higgs bosons to any supersymmetric theory. In the MSSM, we have two chiral supermultiplets. The SM (SUSY) parts of the multiplets are denoted $H_u(\tilde{H}_u)$ and $H_d(\tilde{H}_d)$. Writing out H_u and H_d explicitly:

$$H_u = \begin{pmatrix} H_u^+ \\ H_u^0 \end{pmatrix} \tag{3.6}$$

$$H_d = \begin{pmatrix} H_d^0 \\ H_d^- \end{pmatrix} \tag{3.7}$$

$$\tag{3.8}$$

we see that H_u looks very similar to the SM Higgs with $Y = 1$, and H_d is symmetric to this with $+ \rightarrow -$, with $Y = -1$. The SM Higgs boson, h_0, is a linear superposition of the neutral components of these two doublets. The SUSY parts of the Higgs multiplets, $\tilde{H}_u$ and $\tilde{H}_d$, are each left-handed Weyl spinors. For generic spin-1/2 sparticles, we add the “-ino” suffix. We then call the partners of the two Higgs collectively the *Higgsinos*.

[2] The last one should probably have bigger scare quotes.

Figure 3.1: Particles of the MSSM

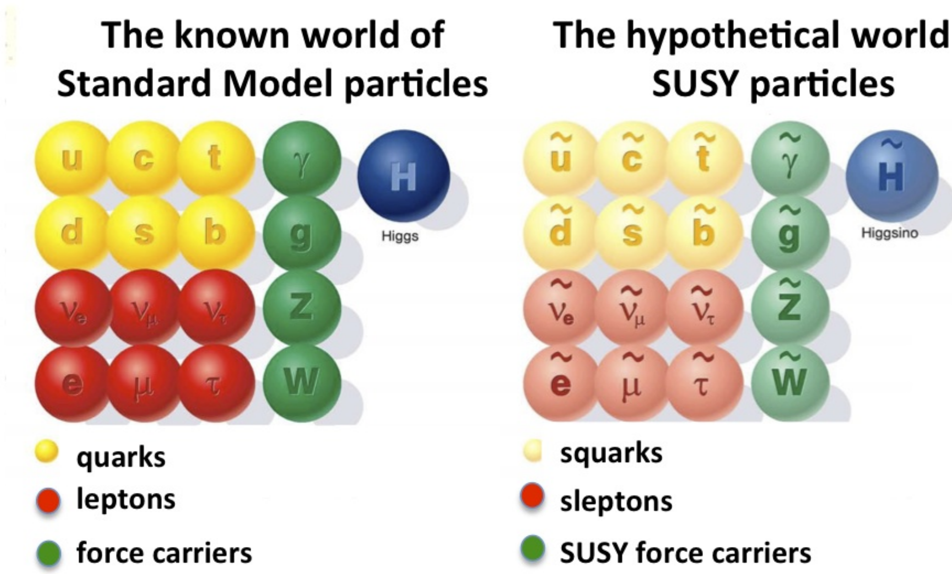

Gauge supermultiplets

The superpartners of the gauge bosons must all be in gauge supermultiplets since they contain a spin-1 particle. Collectively, we refer to the superpartners of the gauge bosons as the gauginos.

The first gauge supermultiplet contains the gluon, and its superpartner, which is known as the *gluino*, denoted $\tilde{g}$. The gluon is of course the SM mediator of $SU(3)_C$; the gluino is also a colored particle, subject to $SU(3)_C$. From the SM before EWSB, we have the four gauge bosons of the electroweak symmetry group $SU(2)_L \otimes U(1)_Y$: $W^{1,2,3}$ and B^0. The superpartners of these particles are thus the *winos* $W^{\tilde{1},2,3}$ and *bino* $\tilde{B}^0$, where each is placed in another gauge supermultiplet with its corresponding SM particle. After EWSB, without breaking supersymmetry, we would also have the zino $\tilde{Z}^0$ and photino $\tilde{\gamma}$.

The entire particle content of the MSSM can be seen in Fig.3.1.

At this point, it's important to take a step back. Where are these particles? As stated above, supersymmetric theories require that the masses and all quantum

Figure 3.2: This Feynmann diagram shows how proton decay is induced in the MSSM, if one does not impose $R-$parity.

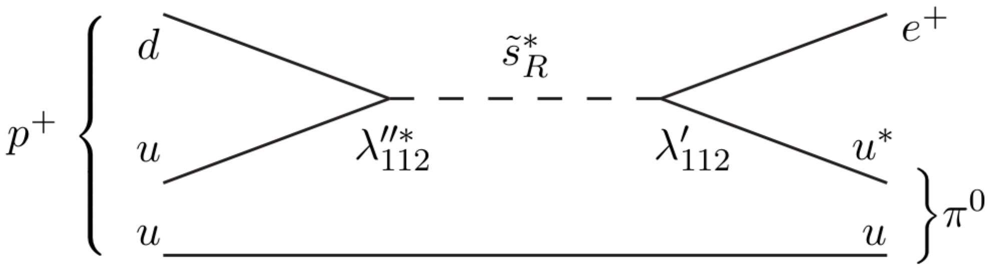

numbers of the SM particle and its corresponding sparticle are the same. Of course, we have not observed a selectron, squark, or wino. The answer, as it often is, is that supersymmetry is *broken* by the vacuum state of nature [15].

$R-$parity

This section is a quick aside to the general story. $R-parity$ refers to an additional discrete symmetry which is often imposed on supersymmetric models. For a given particle state, we define

$$R = (-1)^{3(B-L)+2s} \tag{3.9}$$

where B, L is the baryon (lepton) number and s is the spin. The imposition of this symmetry forbids certain terms from the MSSM Lagrangian that would violate baryon and/or lepton number. This is required in order to prevent proton decay, as shown in Fig.3.2[3]. .

In supersymmetric models, this is a $\mathbb{Z}_2$ symmetry, where SM particles have $R = 1$ and sparticles have $R = -1$. We will take $R-parity$ as part of the definition of the MSSM. We will discuss later the *drastic* consequences of this symmetry on SUSY phenomenology

[3]Proton decay can actually be prevented by allowing only one of the four potential R-parity violating terms to survive.

Soft supersymmetry breaking

The fundamental idea of *soft* supersymmetry breaking[15, 34, 35, 72, 73] is that we would like to break supersymmetry without reintroducing the quadratic divergences we discussed at the end of Chapter 2. We write the Lagrangian in a form :

$$\mathcal{L}_{\text{MSSM}} = \mathcal{L}_{\text{SUSY}} + \mathcal{L}_{\text{soft}} \tag{3.10}$$

In this sense, the symmetry breaking is "soft", since we have separated out the completely symmetric terms from those soft terms which will not allow the quadratic divergences to the Higgs mass.

The explicitly allowed terms in the soft-breaking Lagrangian are [35].

- Mass terms for the scalar components of the chiral supermultipletss
- Mass terms for the Weyl spinor components of the gauge supermultipletss
- Trilinear couplings of scalar components of chiral supermultiplets

In particular, using the field content described above for the MSSM, the softly-broken portion of the MSSM Lagrangian can be writen

$$\begin{aligned}
\mathcal{L}_{\text{soft}} = &-\frac{1}{2}\left(M_3\tilde{g}\tilde{g} + M_2\tilde{W}\tilde{W} + M_1\tilde{B}\tilde{B} + c.c.\right) && (3.11)\\
&-\left(\tilde{u}a_u\tilde{Q}H_u - \tilde{d}a_d\tilde{Q}H_d - \tilde{e}a_e\tilde{L}H_d + c.c.\right) && (3.12)\\
&-\tilde{Q}^\dagger m_Q^2\tilde{Q} - \tilde{L}^\dagger m_L^2\tilde{L} - \tilde{u}m_u^2\tilde{u}^\dagger - \tilde{d}m_d^2\tilde{d}^\dagger - \tilde{e}m_e^2\tilde{e}^\dagger && (3.13)\\
&-m_{H_u}^2 H_u^* H_u - m_{H_d}^2 H_d^* H_d - (bH_uH_d + cc). && (3.14)
\end{aligned}$$

where we have introduced the following notations :

1. M_3, M_2, M_1 are the gluino, wino, and bino masses.
2. a_u, a_d, a_e are complex 3×3 matrices in family space.
3. $m_Q^2, m_u^2, m_d^2, m_L^2, m_e^2$ are hermitian 3×3 matrices in family space.

4. $m^2_{H_u}, m^2_{H_u}, b$ are the SUSY-breaking contributions to the Higgs potential.

We have written matrix terms without any sort of additional notational decoration to indicate their matrix nature, and we now show why. The first term 1 are straightforward; these are just the straightforward mass terms for these fields. There are strong constraints on the off-diagonal terms for the matrices of 2 [74, 75]; for simplicity, we will assume that each $a_i, i = u, d, e$ is proportional to the Yukawa coupling matrix : $a_i = A_{i0} y_i$. The matrices in **??** can be similarly constrained by experiments [68, 75–82] Finally, we assume that the elements 4 contributing to the Higgs potential as well as all of the 1 terms must be real, which limits the possible CP-violating interactions to those of the Standard Model. We thus only consider flavor-blind, CP-conserving interactions within the MSSM.

The important mixing for mass and gauge interaction eigenstates in the MSSM occurs within electroweak sector, in a process akin to EWSB in the Standard Model. The neutral portions of the Higgsinos doublets and the neutral gauginos ($\tilde{H}^0_u, \tilde{H}^0_d, \tilde{B}^0, \tilde{W}^0$ of the gauge interaction basis mix to form what are known as the *neutralinos* of mass basis :

$$M_{\tilde{\chi}} = \begin{pmatrix} M_1 & 0 & -c_\beta s_W m_Z & s_\beta s_W m_Z \\ 0 & M_2 & c_\beta c_W m_Z & -s_\beta c_W m_Z \\ -c_\beta s_W m_Z & c_\beta c_W m_Z & 0 & -\mu \\ s_\beta s_W m_Z & -s_\beta c_W m_Z & -\mu & 0 \end{pmatrix} \tag{3.15}$$

where $s(c)$ are the sine and cosine of angles related to EWSB, which introduced masses to the gauginos and higgsinos. Diagonalization of this matrix gives the four neutralino mass states, listed without loss of generality in order of increasing mass : $\tilde{\chi}^0_{1,2,3,4}$.

The neutralinos, especially the lightest neutralino $\tilde{chi}^0_1$, are important ingredients in SUSY phenomenology.

The same process can be done for the electrically charged gauginos with the charged portions of the Higgsino doublets along with the charged winos ($\tilde{H_u^+}, \tilde{H_d^+}, \tilde{W^+}, \tilde{W^-}$. This leads to the *charginos*, again in order of increasing mass : $\tilde{\chi}^{\pm}_{1,2}$.

3.3 Phenomenology

We are finally at the point where we can discuss the phenomenology of the MSSM, in particular as it manifests itself at the energy scales of the LHC.

As noted above in Sec.3.2, the assumption of $R-$parity has important consequences for MSSM phenomenology. The SM particles have $R = 1$, while the sparticles all have $R = -1$. Simply, this is the "charge" of supersymmetry. Since the particles of LHC collisions (pp) have total incoming $R = 1$, we must expect that all sparticles will be produced in *pairs*. An additional consequence of this symmetry is the fact that the lightest supersymmetric particle (LSP) is *stable*. Off each branch of the Feynmann diagram shown in Fig., we have $R = -1$, and this can only decay to another sparticle and a SM particle. Once we reach the lightest sparticle in the decay, it is absolutely stable. This leads to the common signature $E_{\mathrm{T}}^{\mathrm{miss}}$ for a generic SUSY signal.

For this thesis, we will be presenting an inclusive search for squarks and gluinos with zero leptons in the final state. This is a very interesting decay channel[4], due to the high cross-sections of $\tilde{g}\tilde{g}$ and $\tilde{q}\tilde{q}$ decays, as can be seen in Fig.**??** [83]. This is a direct consequence of the fact that these are the colored particles of the MSSM. Since the sparticles interact with the gauge groups of the SM in the same way as their SM partners, the colored sparticles, the squarks and gluinos, are produced and decay as governed by the color group $SU(3)_C$ with the strong coupling g_S. The digluino production is particularly copious, due to color factor corresponding to the color octet

[4]Prior to Run1, probably the most *most* interesting SUSY decay channel.

Figure 3.3: SUSY signals considered in this thesis

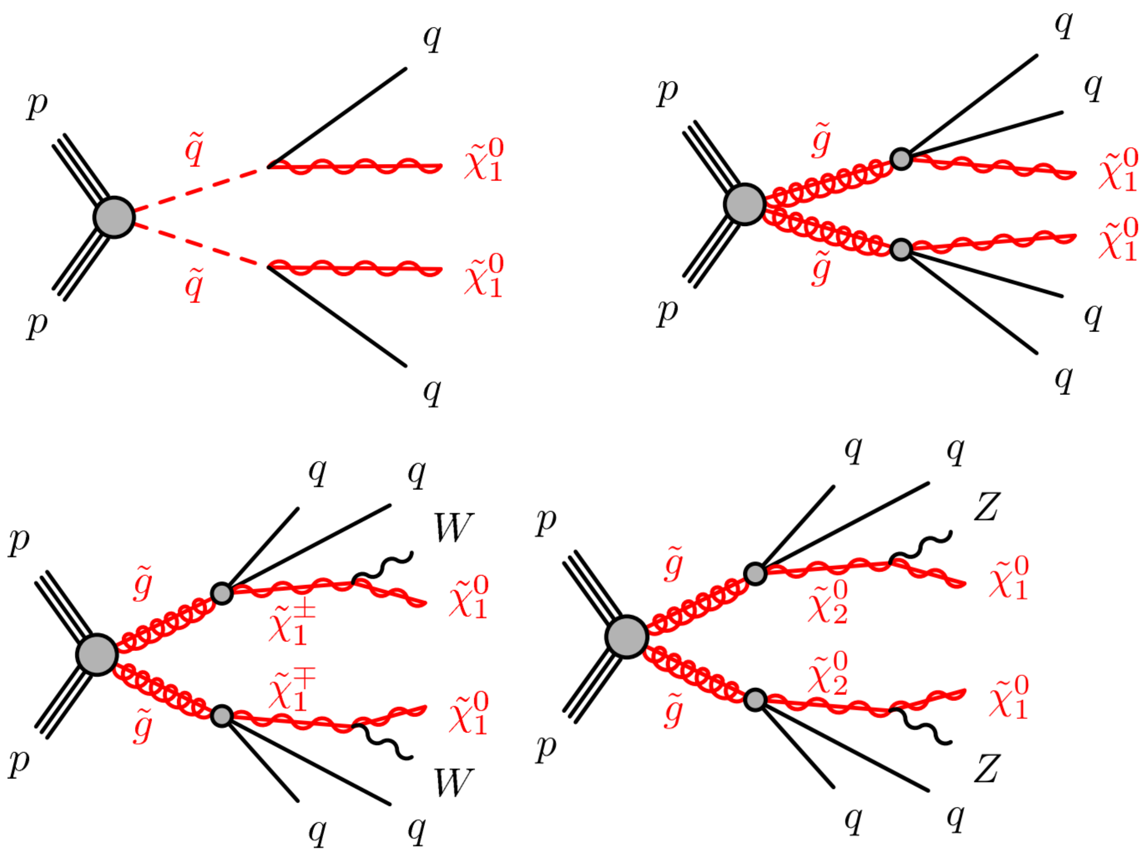

of $SU(3)C$.

In the case of disquark production, the most common decay mode of the squark in the MSSM is a decay directly to the LSP plus a single SM quark [15]. This means the basic search strategy of disquark production is two jets from the final state quarks, plus missing transverse energy for the LSPs. There are also cascade decays, the most common of which, and the only one considered in this thesis, is $\tilde{q} \to q\tilde{\chi}^{\pm} \to qW^{\pm}\chi^0$.

For digluino production, the most common decay is $\tilde{g} \to g\tilde{q}$, due to the large g_S coupling. The squark then decays as listed above. In this case, we generically search for four jets and missing transverse energy from the LSPs. We can also have the squark decay in association with a $W^{\pm}$ or Z^0; in this thesis, we are interested in those cases where this vector boson goes hadronically.

In the context of experimental searches for SUSY, we often consider *simplified*

Figure 3.4: SUSY production cross-sections as a function of sparticle mass at $\sqrt{s} =$ 13 TeV.

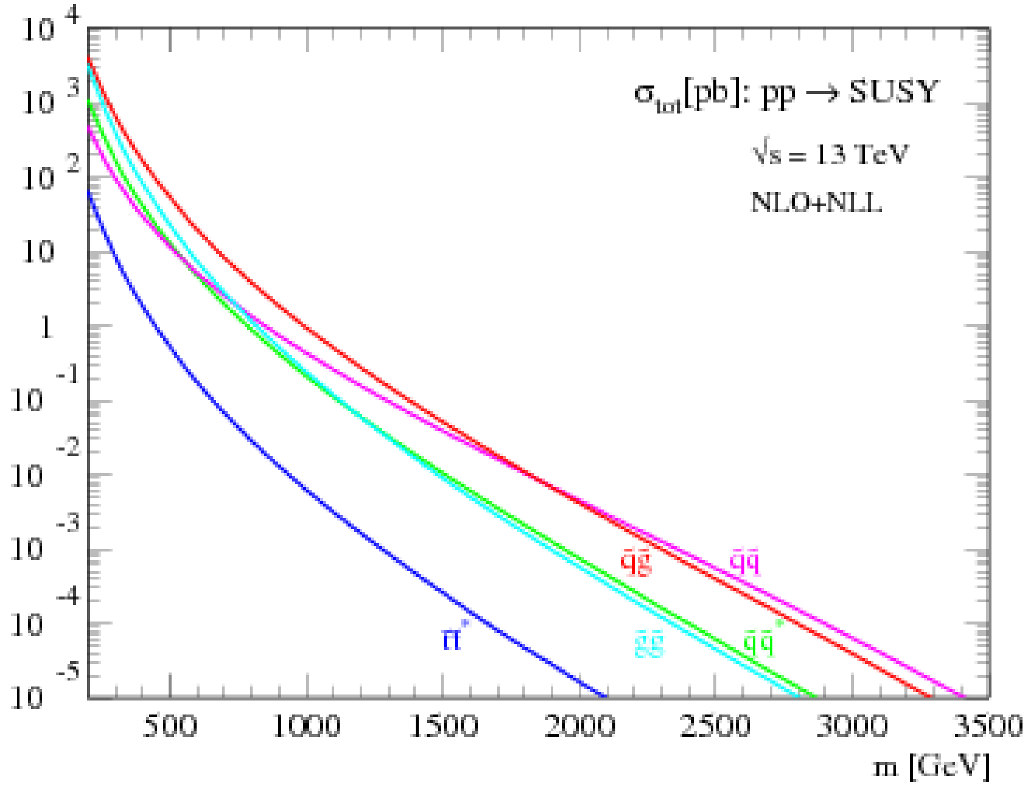

models. These models make certain assumptions which allow easy comparisons of results by theorists and rival experimentalists. In the context of this thesis, the simplified models will make assumptions about the branching ratios described in the preceding paragraphs. In particular, we will often choose a model where the decay of interest occurs with 100% branching ratio. This is entirely for ease of interpretation by other physicists[5], but it is important to recognize that these are more a useful comparison tool, especially with limits, than a strict statement about the potential masses of sought-after beyond the Standard Model particle.

[5]In the author's opionion, this often leads to more confusion than comprehension. We will revisit the shortcomings of simplified models in the Conclusion to this thesis.

Figure 3.5: Loop diagrams correct the Higgs mass in the MSSM

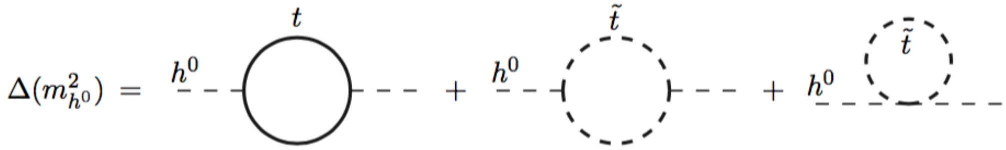

3.4 How SUSY solves the problems with the SM

We now return to the issues with the Standard Model as described in Ch.2 to see how these issues are solved by supersymmetry.

Quadratic divergences to the Higgs mass

The quadratic divergences induced by the loop corrections to the Higgs mass, for example from the top Yukawa coupling, goes as

$$\delta m_H^2 \approx \left(\frac{m_t}{8\pi^2 {<}\phi{>}_{VEV}}\right)^2 \Lambda^2_{Planck}. \tag{3.16}$$

The miraculous thing about SUSY is each of these terms *automatically* comes with a term which exactly cancels this contribution[15]. The fermions and bosons have opposite signs in this loop diagram to all orders in pertubation theory, which completely solves the hierarchy problem. This is the most well-motivated reason for supersymmetry.

Gauge coupling unification

An additional motivation for supersymmetry is seen by the gauge coupling unification high scales. In the Standard Model, as we saw the gauge couplings fail to unify at high energies. In the MSSM and many other forms of supersymmetry, the gauge couplings unify at high energy, as can be seen in Fig.??. This provides additional aesthetic motivation for supersymmetric theories.

Figure 3.6: The running of Standard Model gauge couplings; compare to Fig.2.4. The MSSM gauge couplings nearly intersect at high energies.

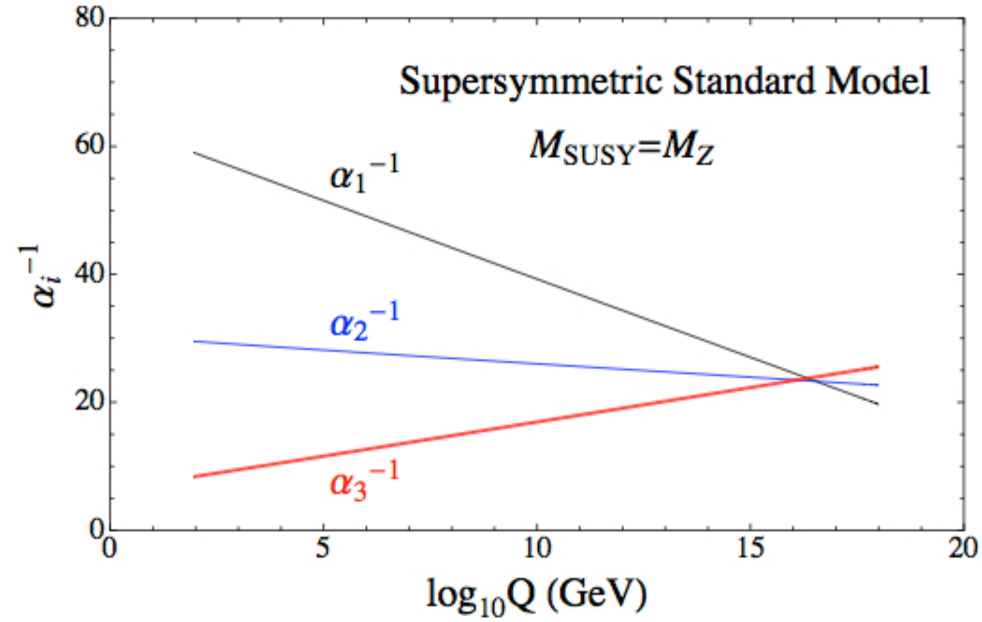

Dark matter

As we discussed previously, the lack of any dark matter candidate in the Standard Model naturally leads to beyond the Standard Model theories. In the Standard Model, there is a natural dark matter candidate in the lightest supersymmetric particle[15] The LSP would in dark matter experiments be called a *weakly-interacting massive particle* (WIMP), which is a type of cold dark matter [22, 84]. These WIMPS would only interact through the weak force and gravity, which is exactly as a model like the MSSM predicts for the neutralino. In Fig.3.7, we can see the current WIMP exclusions for a given mass. The range of allowed masses which have not been excluded for LSPs and WIMPs have significant overlap. This provides additional motivation outside of the context of theoretical details.

Figure 3.7: WIMP exclusions from direct dark matter detection experiments.

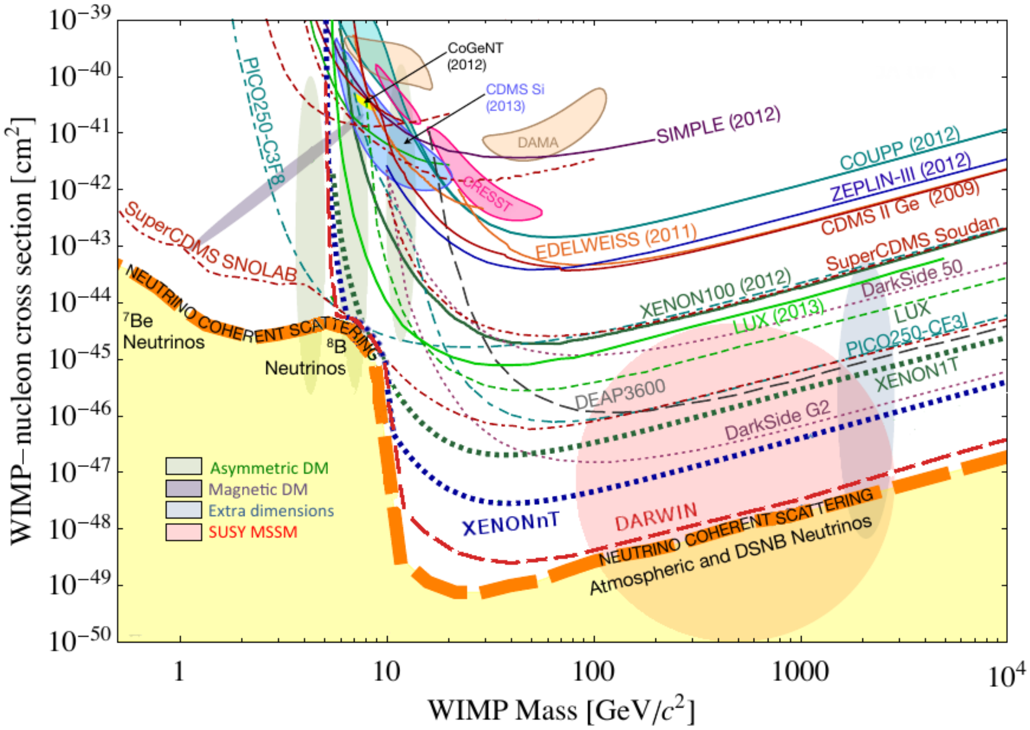

3.5 Conclusions

Supersymmetry is the most well-motivated theory for physics beyond the Standard Model. It provides a solution to the hierarchy problem, leads to gauge coupling unification, and provides a dark matter candidate consistent with galatic rotation curves. As noted in this chapter, due to the LSPs in the final state, most SUSY searches require a significant amount of missing transverse energy in combination with jets of high transverse momentum. However, there is some opportunity to do better than this, especially in final states where one has two weakly-interacting LSPs on opposite sides of some potentially complicated decay tree. We will see how this is done in Ch.??.

Chapter 4

The Large Hadron Collider

The Large Hadron Collider (LHC) produces high-energy protons which are collided at the center of multiple large experiments at CERN on the outskirts of Geneva, Switzerland [85]. The LHC produces the highest energy collisions in the world, with design center-of-mass energy of $\sqrt{s} = 14$ TeV, which allows the experiments to investigate physics far beyond the reach of previous colliders. This chapter will summarize the basics of accelerator physics, especially with regards to discovering physics beyond the Standard Model. We will describe the CERN accelerator complex and the LHC.

4.1 Basics of Accelerator Physics

This section follows closely the presentation of [86].

Simple particle accelerators simply rely on the acceleration of charged particles in a static electric field. Given a field of strength E, charge q, and mass m, this is simply

$$a = \frac{qE}{m}. \tag{4.1}$$

For a given particle with a given mass and charge, this is limited by the static electric field which can be produced, which in turn is limited by electrical breakdown at high voltages.

There are two complementary solutions to this issue. First, we use the *radio frequency acceleration* technique. We call the devices used for this *RF cavities*. The cavities produce a time-varied electric field, which oscillate such that the charged particles passing through it are accelerated towards the design energy of the RF cavity. This oscillation also induces the particles into *bunches*, since particles which are slightly off in energy from that induced by the RF cavity are accelerated towards the design energy.

Second, one bends the particles in a magnetic field, which allows them to pass through the same RF cavity over and over. This second process is often limited by *synchrotron radiation*, which describes the radiation produced when a charged particle is accelerated. The power radiated is

$$P \sim \frac{1}{r^2}\Big(E/m\Big)^4 \tag{4.2}$$

where r is the radius of curvature and E, m is the energy (mass) of the charged particle. Given an energy which can be produced by a given set of RF cavities (which is *not* limited by the mass of the particle), one then has two options to increase the actual collision energy : increase the radius of curvature or use a heavier particle. Practically speaking, the easiest options for particles in a collider are protons and electrons, since they are (obviously) copious in nature and do not decay[1]. Given the dependence on mass, we can see why protons are used to reach the highest energies. The tradeoff for this is that protons are not point particles, and we thus we don't know the exact incoming four-vectors of the protons, as discussed in Ch.2.

The particle *beam* referes to the bunches all together An important property of a beam of a particular energy E, moving in uniform magnetic field B, containing particles of momentum p is the *beam rigidity* :

$$R \equiv rB = p/c. \tag{4.3}$$

The linear relation between r and p, or alternatively B and p have important consequences for LHC physics. For hadron colliders, this is the limiting factor on

[1]Muon colliders are a really cool option at high energies, since the relativistic γ factor gives them a relatively long lifetime in the lab frame.

going to higher energy scales; one needs a proportionally larger magnetic field to keep the beam accelerating in a circle.

Besides the rigidity of the beam, the most important quantities to characterize a beam are known as the (normalized) *emittance* ϵ_N and the *betatron function* β. These quantities determine the transverse size σ of a relativistic beam $v \stackrel{\sim}{<} c$ beam : $\sigma^2 = \beta^* \epsilon_N / \gamma_{\text{rel}}$, where β^* is the value of the betatron function at the collision point and γ_{rel} is the Lorentz factor.

These quantities determine the *instaneous luminosity* L of a collider, which combined with the cross-section σ of a particular physics process, give the rate of this physics process :

$$R = L\sigma. \tag{4.4}$$

The instaneous luminosity L is given by :

$$L = \frac{f_{\text{rev}} N_b^2 F}{4\pi\sigma^2} = \frac{f_{\text{rev}} n N_b^2 \gamma_{\text{rel}} F}{4\pi\beta^* \epsilon_N}. \tag{4.5}$$

Here we have introduced the frequency of revolutions f_{rev}, the number of bunches n, the number of protons per bunch N_b^2, and a geometric factor F related to the crossing angle of the beams.

The *integrated luminosity* $\int L$ gives the total number of a particular physics process P, with cross-section σ_{P}.

$$N_{\text{P}} = \sigma_{\text{P}} \int L. \tag{4.6}$$

Due to this simple relation, one can also quantify the "amount of data delivered" by a collider simply by $\int L$.

4.2 Accelerator Complex

The Large Hadron Collider is the last accelerator in a chain of accelerators which together form the CERN accelerator complex, which can be seen in 4.1. The protons

Figure 4.1: The CERN accelerator complex.

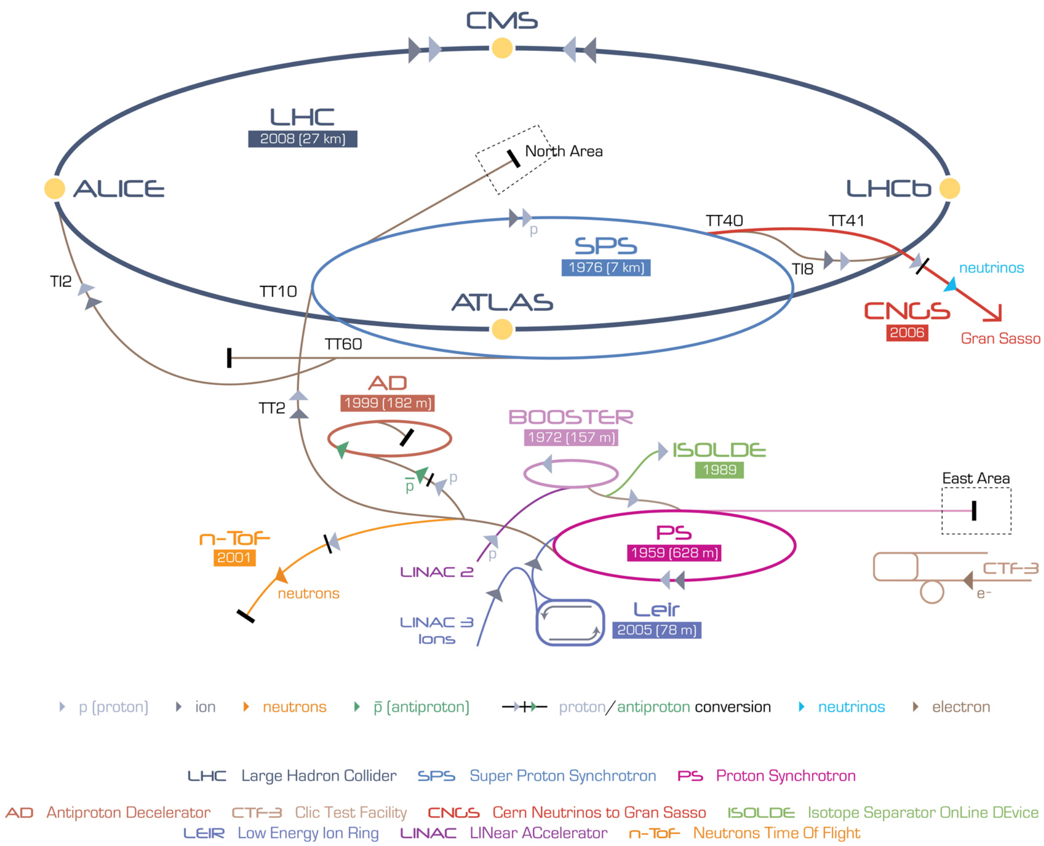

begin their journey to annilation in a hydrogen source, where they are subsequently ionized. The first acceleration occurs in the Linac 2, a linear accelerator composed of RF cavities. The protons leave the Linac 2 at an energy of 50 MeV and enter the Proton Synchrotron Booster (PSB). The PSB contains four superimposed rings, which accelerate the protons to 1.4 GeV. The protons are then injected into the Proton Synchrotron (PS). This synchrotron increases the energy up to 25 GeV. After leaving the PS, the protons enter the Super Proton Synchrotron (SPS). This is the last step before entering the LHC ring, and the protons are accelerated to 450 GeV. From the SPS, the protons are injected into the beam pipes of the LHC. The process to fill the LHC rings with proton bunches from start to finish typically takes about four minutes.

4.3 Large Hadron Collider

The Large Hadron Collider is the final step in the CERN accelerator complex, and produces the collisions analyzed in this thesis. From the point of view of experimentalists on the general-purpose ATLAS and CMS experiments, the main goal of the LHC is to deliver collisions at the highest possible energy, with the highest possible instaneous luminosity. The LHC was installed in the existing 27 km tunnel used by the Large Electron Positron (LEP) collider [87]. This allowed the existing accelerator complex at CERN, described in the previous section, to be used as the injection system to prepare the protons up to 450 GeV. Many aspects of the LHC design were decided by this very fact, and specified the options allowed to increase the energy or luminosity. In particular, the radius of the tunnel was already specified; from Eq.4.3, this implies the momentum (or energy) of the beam is entirely determined by the magnetic field. Given the 27 km circumference of the LEP tunnel, one can calculate the required magnetic field to reach the 7 TeV per proton design energy of the LHC :

$$r = C/2\pi = 4.3 \text{ km} \tag{4.7}$$

$$\rightarrow B = \frac{p}{rc} = 5 \text{ T} \tag{4.8}$$

In fact, the LHC consists of 8 528 m straight portions consisting of RF cavities, used to accelerate the particles, and 8 circular portions which bend the protons around the LHC ring. These circular portions actually have a slightly smaller radius of curvature $r = 2804$ m, and we require $B = 8.33$ T. To produce this large field, we need to use superconducting magnets, as discussed in the next section.

Magnets

There are many magnets used by the LHC machine, but the most important are the 1232 dipole magnets; a schematic is shown in Fig.4.2 and a photograph is shown in

Figure 4.2: Schematic of an LHC dipole magnet.

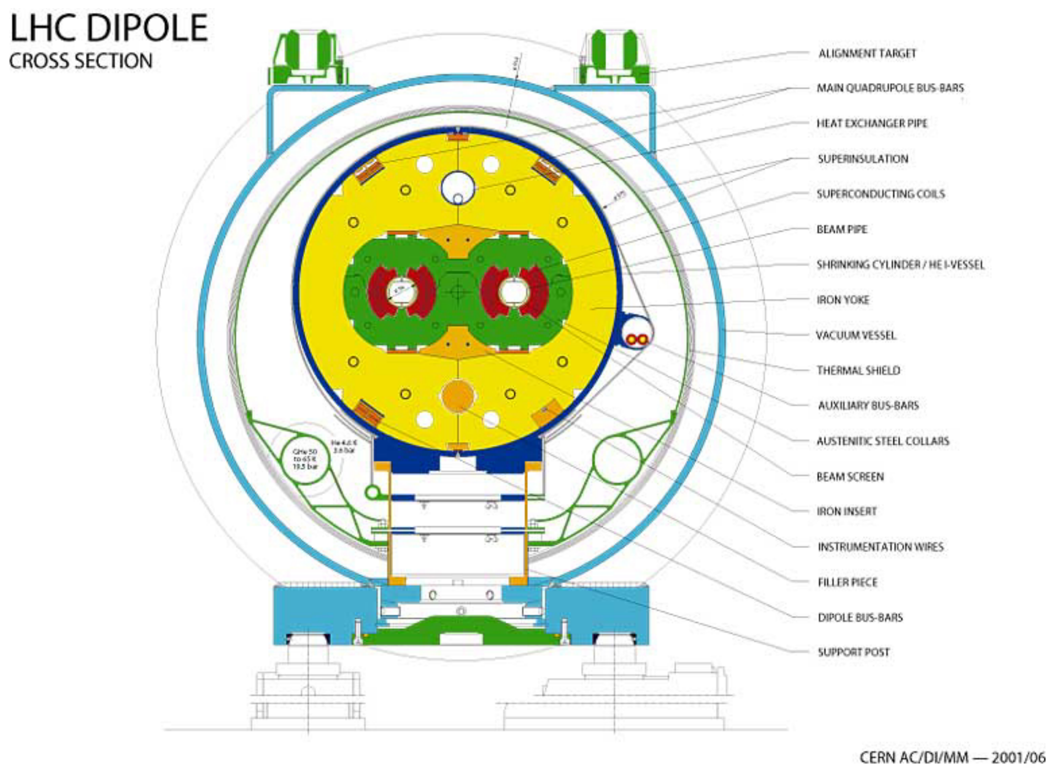

Fig.4.3.

The magnets are made of Niobium and Titanium. The maximum field strength is 10 T when cooled to 1.9 Kelvin. The magnets are cooled by superfluid helium, which is supplied by a large cryogenic system. Due to heating between the eight helium refrigerators and the beampipe, the helium is cooled in the refrigerators to 1.8 K.

A failure in the cooling system can cause what is known as a *quench*. If the temperature goes above the critical superconducting temperature, the metal loses its superconducting properties, which leads to a large resistance in the metal. This leads to rapid temperature increases, and can cause extensive damages if not controlled.

The dipole magnets are 16.5 meters long with a diameter of 0.57 meters. There are two individual beam pipes inside each magnet, which allows the dipoles to house the beams travelling in both directions around the LHC ring. They curve slightly, at an angle of 5.1 mrad, which carefully matches the curvature of the ring. The

Figure 4.3: Photograph of a technician connecting an LHC dipole magnet.

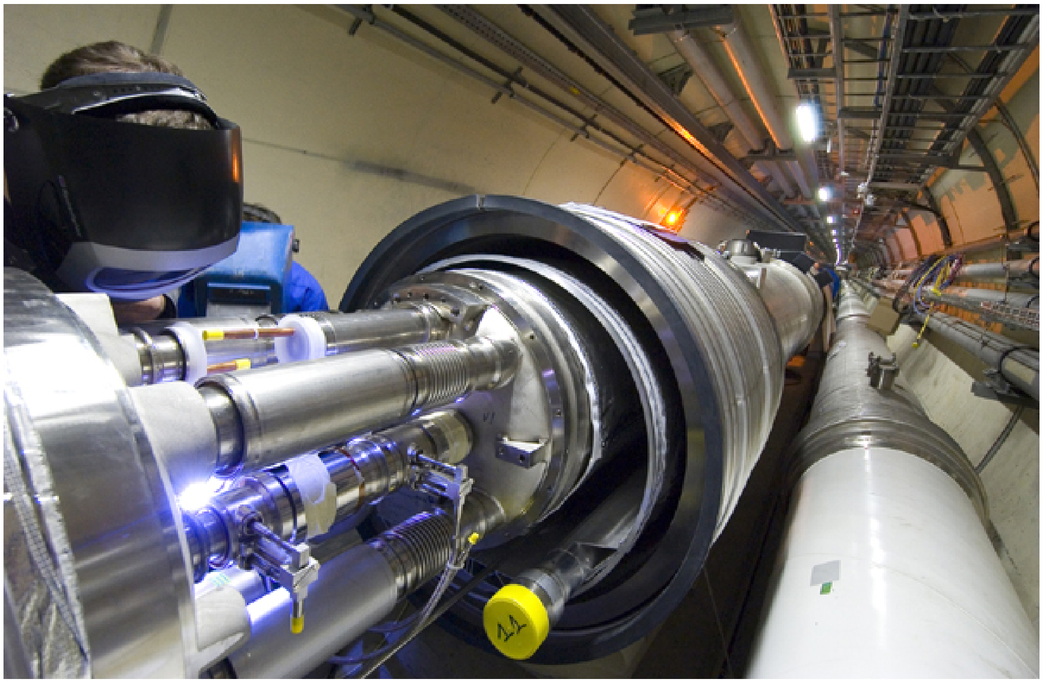

beampipes inside of the magnets are held in high vacuum, to avoid stray particles interacting with the beam.

4.4 Dataset Delivered by the LHC

In this thesis, we analyze the data delivered by the LHC to ATLAS in the 2015 and 2016 datasets. The beam parameters relevant to this dataset are available in Table 4.1.

The peak instaneous luminosity delivered in 2015 (2016) was $L = 5.2\,(11)\,\mathrm{cm}^{-2}\mathrm{s}^{-1} \times 10^{33}$. One can note that the instaneous luminosity delivered in the 2016 dataset exceeds the design luminosity of the LHC. The total integrated luminosity delivered was $13.3\,\mathrm{fb}^{-1}$. In Figure 4.4, we display the integrated luminosity as a function of day for 2015 and 2016.

Figure 4.4: Integrated Luminosity delivered by the LHC and collected by ATLAS in the 2015 and 2016 datasets.

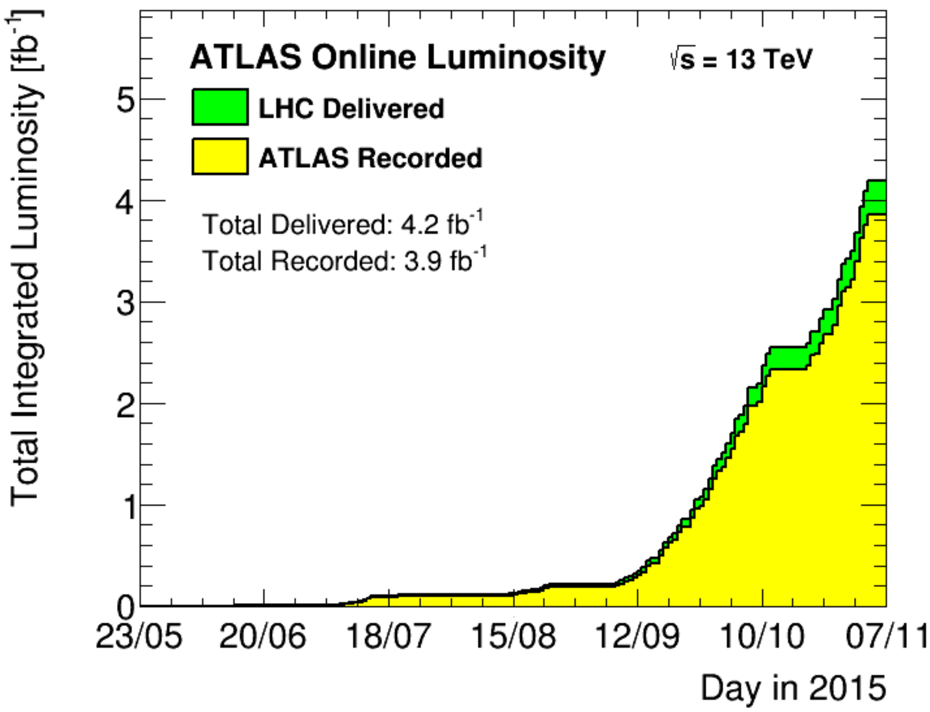

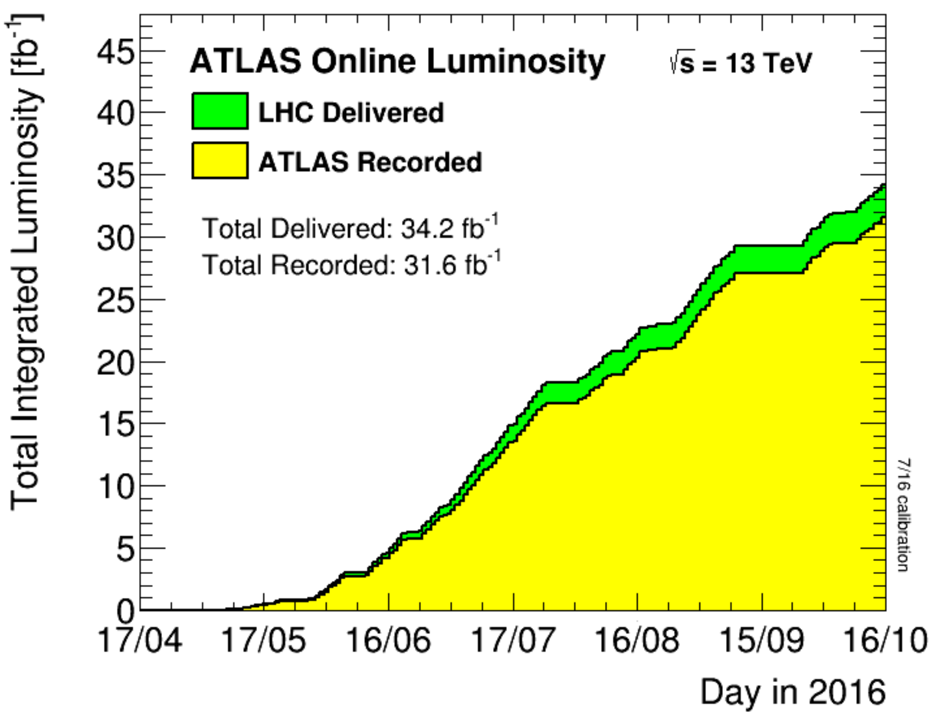

Table 4.1: Beam parameters of the Large Hadron Collider.

Parameter	Injection	Extraction
Energy (GeV)	450	7000
Rigidity (T-m)	3.8	23353
Bunch spacing (ns)	25	25
Design Luminosity ($cm^{-2}s^{-1} \times 10^34$)	-	1.0
Bunches per proton beam	2808	2808
Protons per bunch	1.15 e11	1.15 e11
Beam lifetime (hr)	-	10
Normalized Emittance ϵ_N (mm μrad)	3.3	3.75
Betatron function at collision point β^* (cm)	-	55

Figure 4.5: Simulated event with many pileup vertices.

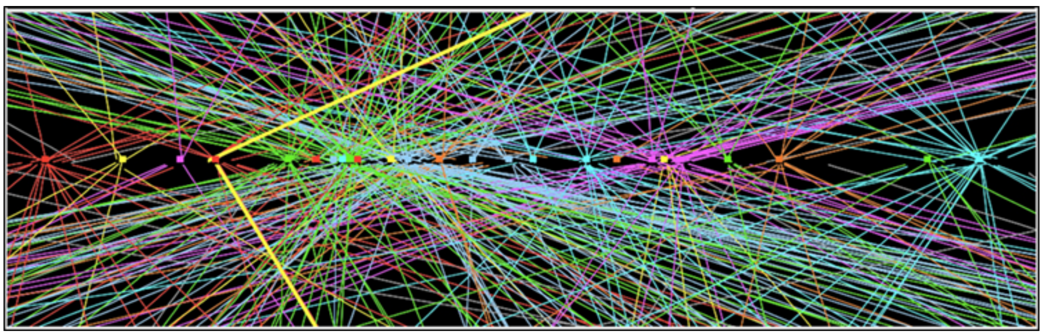

Pileup

Pileup is the term for the additional proton-proton interactions which occur during each bunch crossing of the LHC. At the beginning of the LHC physics program, there had not been a collider which averaged more than a single interaction per bunch crossing. In the LHC, each bunch crossing (or *event*) generally contains multiple proton-proton interactions. An simulated event with many *vertices* can be seen in Fig.4.5. The so-called *primary vertex* (or *hard scatter vertex*) refers to the vertex which has the highest Σp_T^2; this summation occurs over the *tracks* in the detector, which we will describe later[**ATL-INDET-PUB-2009-001**]. We then distinguish between *in-time* pileup and *out-of-time* pileup. In-time pileup refers to the additional proton-proton interactions which occur in the event. Out-of-time pileup refers to effects related to proton-proton interactions previous bunch crossings.

We quantify in-time pileup by the number of "primary"[2] vertices in a particular event. To quantify the out-of-time pileup, we use the average number of interactions per bunch crossing $< \mu >$ over some human-scale time. In Figure 4.6, we show the distribution of μ for the dataset used in this thesis.

[2] *The* primary vertex is as defined above, but we unfortunately use the same name here.

Figure 4.6: Mean number of interactions per bunch crossing in the 2015 and 2016 datasets.

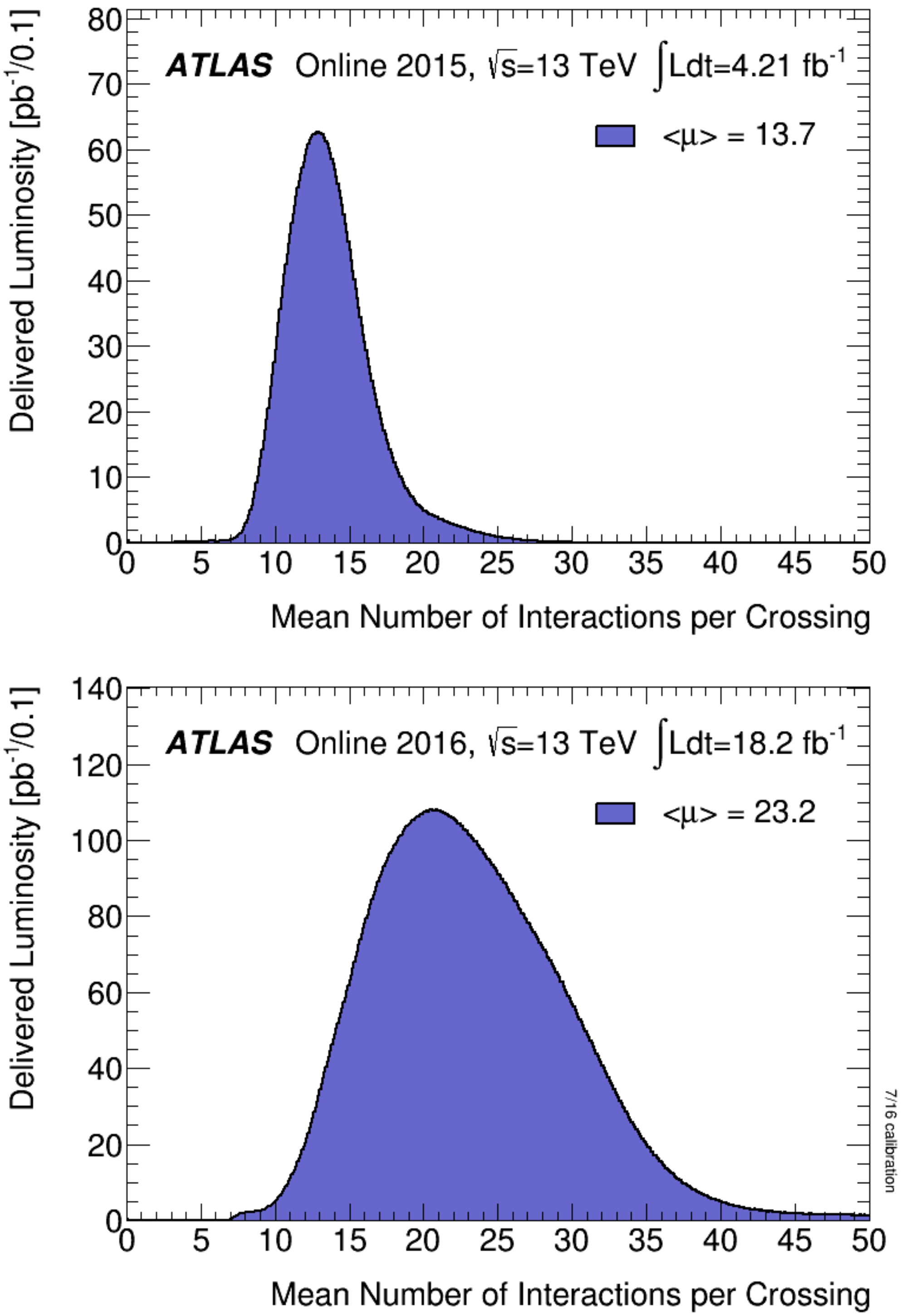

Chapter 5

The ATLAS detector

The dataset analyzed in this thesis was taken by the ATLAS detector [88], which is located at the "Point 1" cavern of the LHC beampipe, just across the street from the main CERN campus. The much-maligned acronym stands for *A T*oriodal *L*HC *A*pparatu*S*. ATLAS is a massive cylindrical detector, with a radius of 12.5 m and a length of 44 m, with nearly hermitic coverage around the collision point. It consists of multiple subdetectors; each plays a role in ATLAS's ultimate purpose of measuring the energy, momentum, and type of the particles produced in collisions delivered by the LHC. These subdetectors are immersed in a hybrid solenoid-toroid magnet system whichs forces charged particles to curve, which allows for precise measurements of their momenta. These magnetic fields are maximized in the central solenoid magnet, which contains a magnetic field of 2 T. A schematic of the detector can be seen in 5.1.

The *inner detector* (ID) lies closest to the collision point, and contains three separate subdetectors. It provides pseudorapidity[1]coverage of $|\eta| < 2.5$ for charged particles to interact with the tracking material. The tracks reconstructed from the inner detector hits are used to reconstruct the primary vertices, as noted in Ch.**??**,

[1] ATLAS uses a right-handed Cartesian coordinate system; the origin is defined by the nominal beam interaction point. The positive-z direction is defined by the incoming beam travelling counterclockwise around the LHC. The positive-x direction points towards the center of the LHC ring from the origin, and the positive-y direction points upwards towards the sky. For particles of transverse (in the $x - y$ plane) momentum $p_T = \sqrt{p_x^2 + p_y^2}$ and energy E, it is generally most convenient fully describe this particle's kinematics as measured by the detector in the (p_T, ϕ, η, E) basis. The angle $\phi = \arctan(p_y/p_x)$ is the standard azimuthal angle, and $\eta = \ln\tan(\theta/2)$ is known as the pseudorapidity, and defined based on the standard polar angle $\theta = \arccos(p_z/p_T)$. For locations of i.e. detector elements, both (r, ϕ, η) and (z, ϕ, η) can be useful.

Figure 5.1: The ATLAS detector

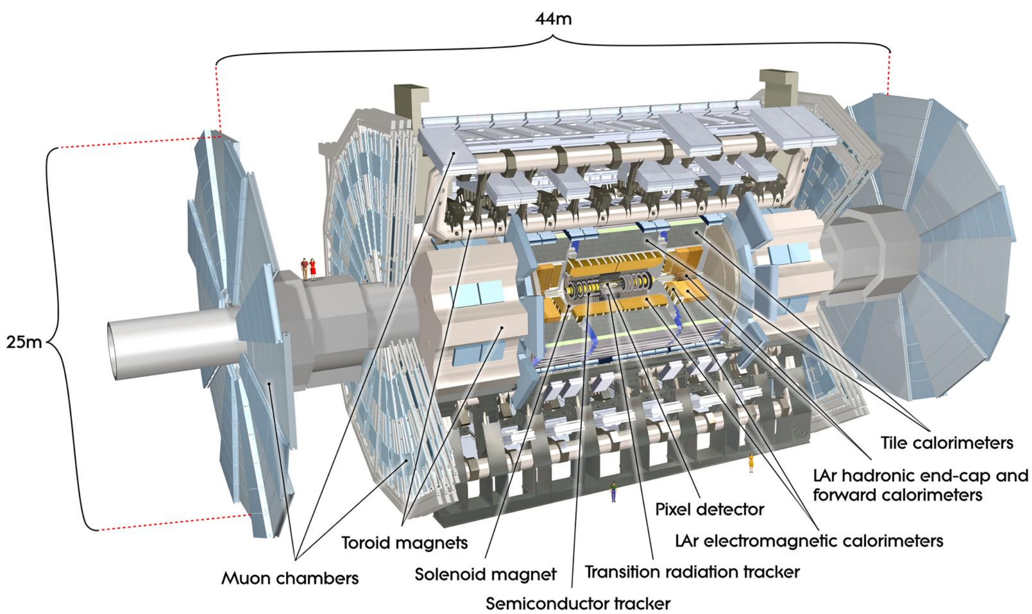

and to determine the momemta of charged particles. The ATLAS *calorimeter* consists of two subdetectors, known as the *electromagnetic* and *hadronic* calorimeters. These detectors stop particles in their detector material, and measure the energy deposition inside, which measures the energy of the particles deposited. The calorimeters provide coverage out to pseudorapidity of $|\eta| < 4.9$. The muon spectrometer is aptly named; it is specifically used for muons, which are the only particles which generally reach the outer portions of the detector. In this region, we have the large tracking systems of the muon spectrometer, which provide precise measurements of muon momenta. The muon spectrometer has pseudorapidity coverage of $|\eta| < 2.7$.

5.1 Magnets

ATLAS contains multiple magnetic systems; primarily, we are concerned with the solenoid, used by the inner detector, and the toroids located outside of the ATLAS calorimeter. A schematic is shown in Fig.5.2. These magnetic fields are used to bend

Figure 5.2: The ATLAS magnet system

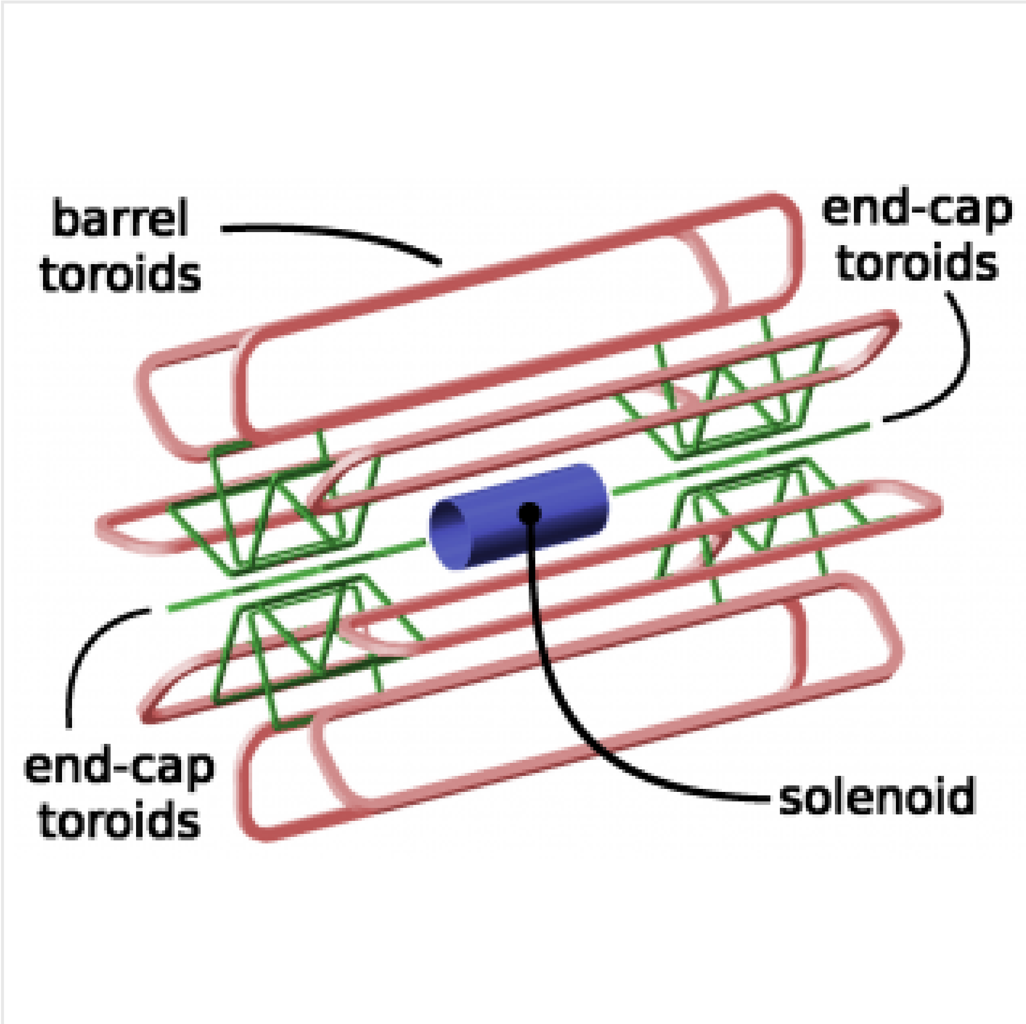

charged particles under the Lorentz force, which subsequently allows one to measure their momentum.

The ATLAS central solenoid is a 2.3 m diameter, 5.3 m long solenoid at the center of the ATLAS detector. It produces a uniform magnetic field of 2 T; this strong field is necessary to accurately measure the charged particles in this field. An important design constraint for the central solenoid was the decision to place it in between the inner detector and the calorimeters. To avoid excessive impacts on measurements in the calorimetry, the central solenoid must be as transparent as possible[2].

[2]This is also one of the biggest functional differences between ATLAS and CMS; in CMS, the

Figure 5.3: The ATLAS inner detector

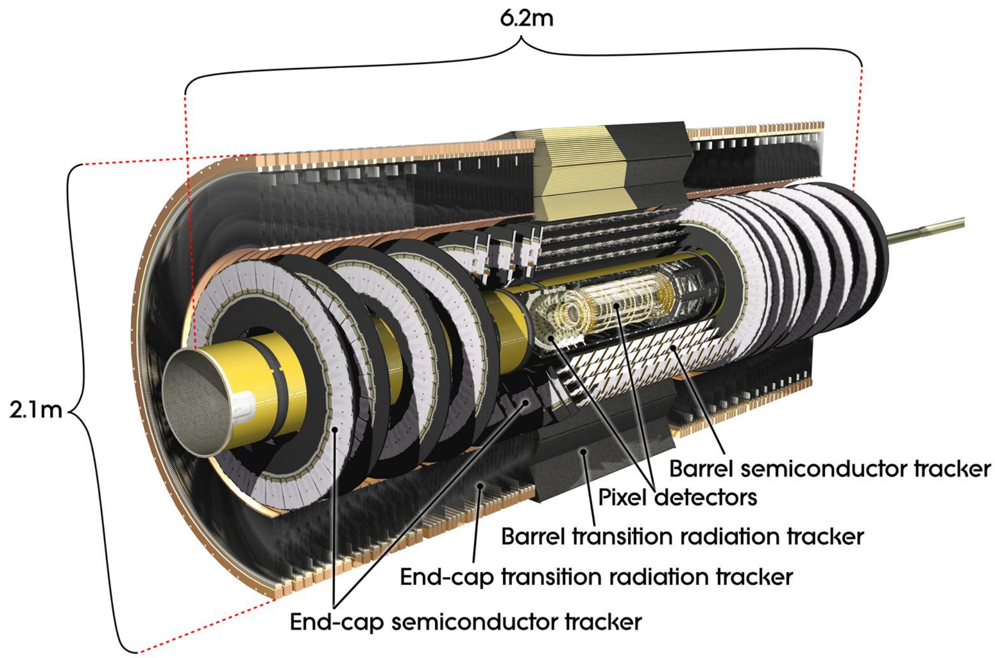

The toroid system consists of eight air-core superconducting barrel loops; these give ATLAS its distinctive shape. There are also two endcap air-core magnets. These produce a magnetic field in a region of approximately 26 m in length and 10 m of radius. The magnetic field in this region is non-uniform, due to the prohibitive costs of a solenoid magnet of that size.

5.2 Inner Detector

The ATLAS inner detector consists of three separate tracking detectors, which are known as, in order of increasing distance from the interaction point, the Pixel Detector, Semiconductor Tracker (SCT), and the Transition Radiation Tracker (TRT). When charged particles pass through these tracking layers, they produce *hits*, which using the known 2 T magnetic field, allows the reconstruction of *tracks*. Tracks are used as inputs for reconstruction of many higher-level physics objects,

solenoid is outside of the calorimeters.

Figure 5.4: The ATLAS pixel detector

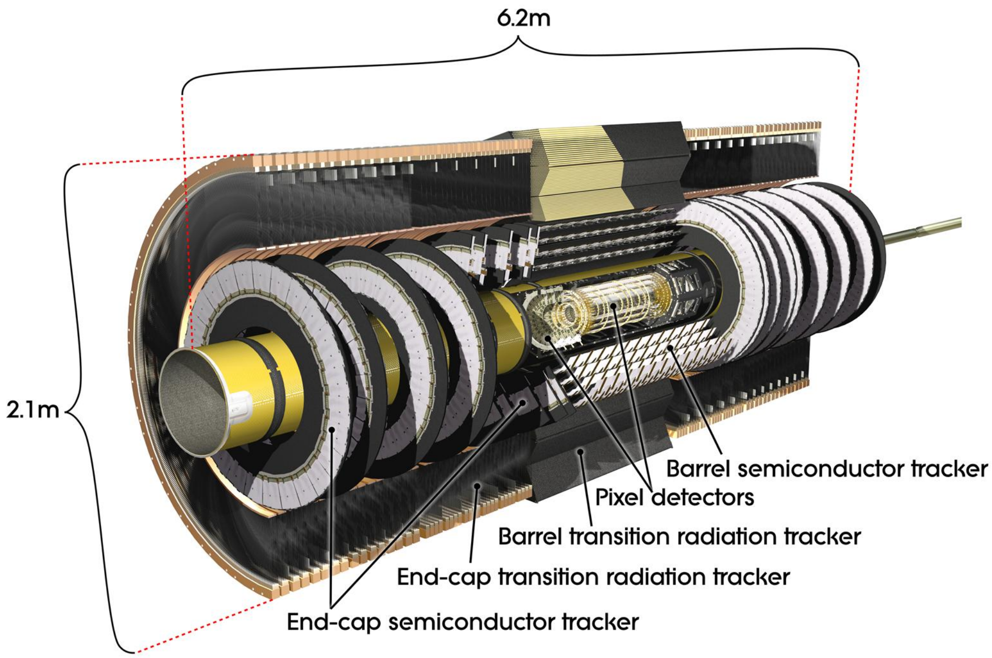

such as electrons, muons, photons, and $E_{\mathrm{T}}^{\mathrm{miss}}$. Accurate track reconstruction is thus crucial for precise measurements of charged particles.

Pixel Detector

The ATLAS pixel detector consists four layers of silicon “pixels”. This refers to the segmentation of the active medium into the pixels; compare to the succeeding silicon detectors, which will use silicon “strips”. This provides precise 3D hit locations. The layers are known as the “Insertable”[3]B-Layer (IBL), the B-Layer (or Layer-0), Layer-1, and Layer-2, in order of increasing distance from the interaction point. These layers are very close to the interaction point, and therefore experience a large amount of radiation.

Layer-1, Layer-2, and Layer-3 were installed with the initial construction of ATLAS. They contain front-end integrated electronics (FEI3s) bump-bonded to 1744

[3] *Very* often, the IBL is mistakenly called the Inner B-Layer, which would have been a much more sensible name.

silicon modules; each module is 250 μm in thickness and contains 47232 pixels. These pixels have planar sizes of 50 x 400 μ^2 or 50 x 600 μ^2, to provide highly accurate location information. The FEI3s are mounted on long rectangular structures known as staves, which encircle the beam pipe. A small tilt to each stave allows full coverage in ϕ even with readout systems which are installed. These layers are at radia of 50.5 mm, 88.5 mm, and 122.5 mm from the interaction point.

The IBL was added to ATLAS after Run1 in 2012 at a radius of 33 mm from the interaction point. The entire pixel detector was removed from the center of ATLAS to allow an additional pixel layer to be installed. The IBL was required to preserve the integrity of the pixel detector as radiation damage leads to inoperative pixels in the other layers. The IBL consists of 448 FEI4 chips, arranged onto 14 staves. Each FEI4 has 26880 pixels, of planar size 50 x 250 μm. This smaller granularity was required due to the smaller distance to the interaction point.

In total, a charged particle passing through the inner detector would expect to leave four hits in the pixel detector.

Semiconductor Tracker

The SCT is directly beyond Layer-2 of the pixel detector. This is a silicon strip detector, which do not provide the full 3D information of the pixel detector. The dual-sensors of the SCT contain 2 x 768 individual strips; each strip has area 6.4 cm^2. The SCT dual-sensor is then double-layered, at a relative angle of 40 mrad; together these layers provide the necessary 3D information for track reconstruction. There are four of these double-layers, at radia of 284 mm, 355 mm, 427 mm, and 498 mm. These double-layers provide hits comparable to those of the pixel detector, and we have four additional hits to reconstruct tracks for each charged particle.

Figure 5.5: A ring of the Semiconductor Tracker

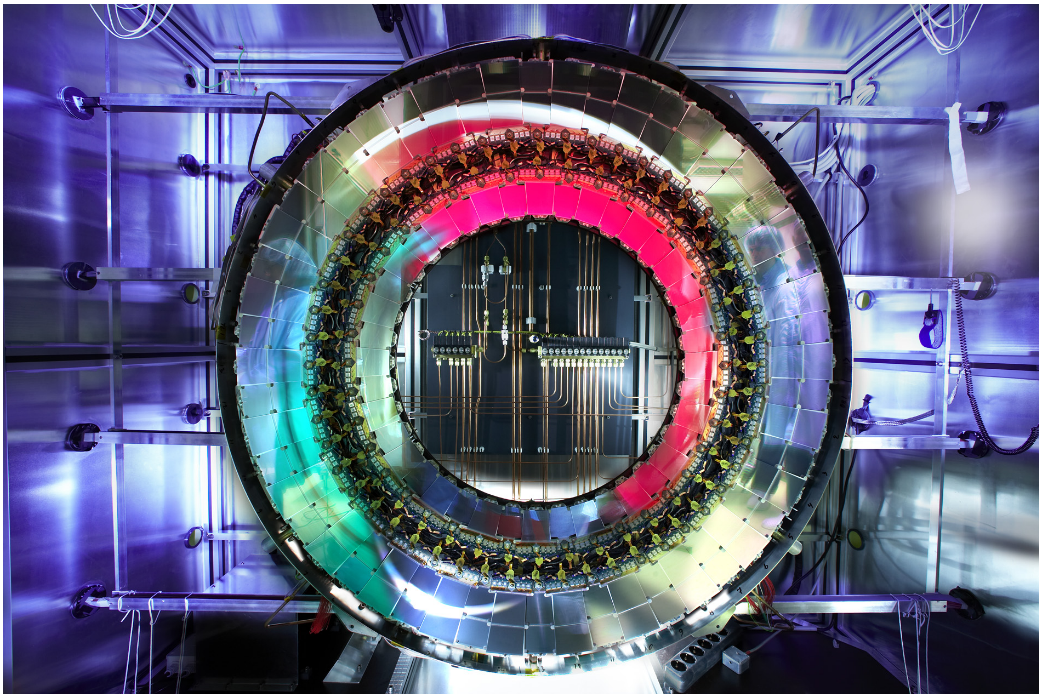

Figure 5.6: A schematic of the Transition Radiation Tracker

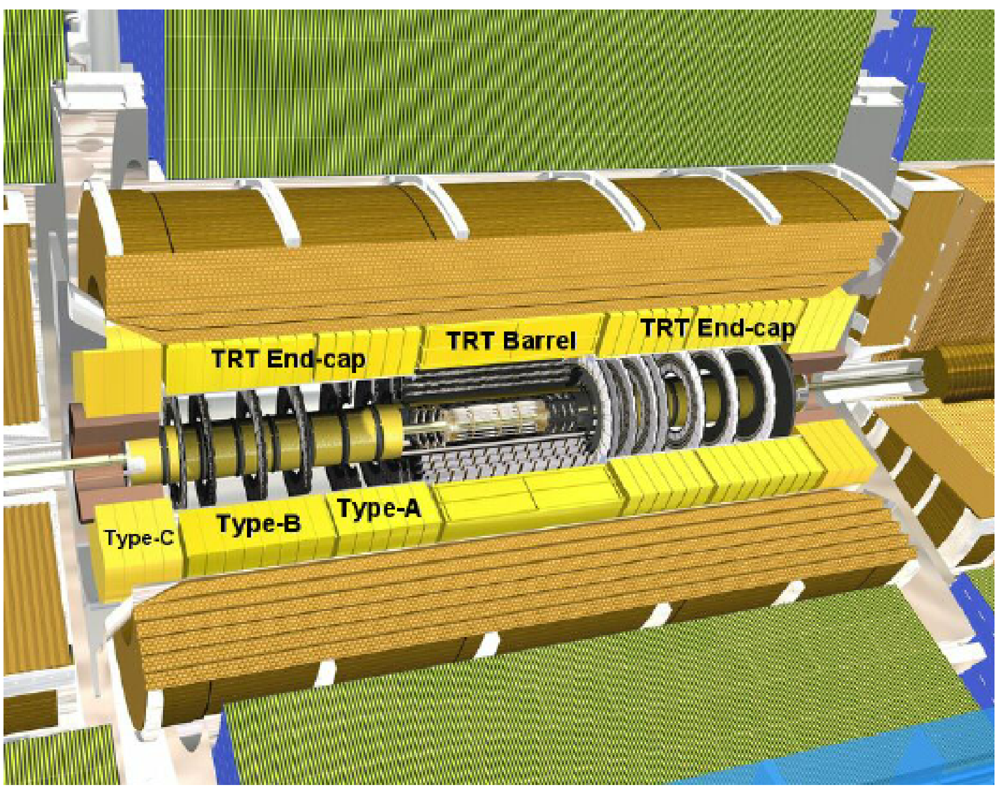

Transition Radiation Tracker

The Transition Radiation Tracker is the next detector radially outward from the SCT. It contains straw drift tubes; these contain a tungsten gold-plated wire of 32 μm diameter held under high voltage (-1530 V) with the edge of the Kapton-aluminum tube. They are filled with a gas mixture of primarily xenon that is ionized when a charged particle passes through the tube. The ions are collected by the "drift" due to the voltage inside the tubes, which is read out by the electronics. This gives so-called "continuous tracking" throughout the tube, due to the large number of ions produced.

The TRT is so-named due to the *transition radiation* (TR) it induces. Due to the dielectric difference between the gas and tubes, TR is induced. This is important for distinguishing electrons from their predominant background of minimum ionizing particles. Generally, electrons have a much larger Lorentz factor than minimum ionizing particles, which leads to additional TR. This can be used as an additional handle for electron reconstruction.

5.3 Calorimetry

The calorimetry of the ATLAS detector also includes multiple subdetectors; these subdetectors allow precise measurements of the electrons, photons, and hadrons produced by the ATLAS detector. Generically, calorimeters work by stopping particles in their material, and measuring the energy deposition. This energy is deposited as a cascade particles induce from interactions with the detector material known *showers*. ATLAS uses *sampling* calorimeters; these alternate a dense absorbing material, which induces showers, with an active layer which measures energy depositions by the induced showers. Since some energy is deposited into the absorption layers as well, the energy depositions must be properly calibrated for the detector.

Figure 5.7: The ATLAS calorimeter

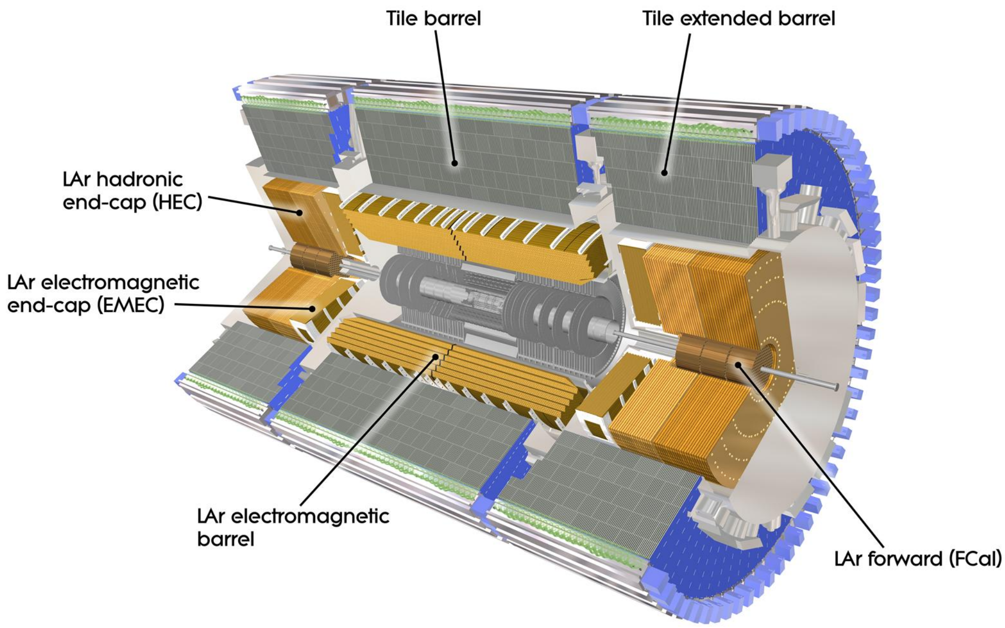

Electromagnetic objects (electrons and photons) and hadrons have much different interaction properties, and thus we need different calorimeters to accurately measure these different classes of objects; we can speak of the *electromagnetic* and *hadronic* calorimeters. ATLAS contains four separate calorimeters : the liquid argon (LAr) electromagnetic barrel calorimeter, the Tile barrel hadronic calorimeter, the LAr endcap electromagnetic calorimeter, the LAr endcap hadronic calorimeter, and the LAr Forward Calorimeter (FCal). Combined, these provide full coverage in ϕ up to $|\eta| < 4.9$, and can be seen in Fig.5.7.

Electromagnetic Calorimeters

The electromagnetic calorimeters of the ATLAS detector consist of the barrel and endcap LAr calorimeters. These are arranged into an ingenious "accordion" shape, shown in 5.8, which allows full coverage in ϕ and exceptional coverage in η while still allowing support structures for detector operation. The accordion is made of

Figure 5.8: A schematic of a subsection of the barrel LAr electromagnetic calorimeter

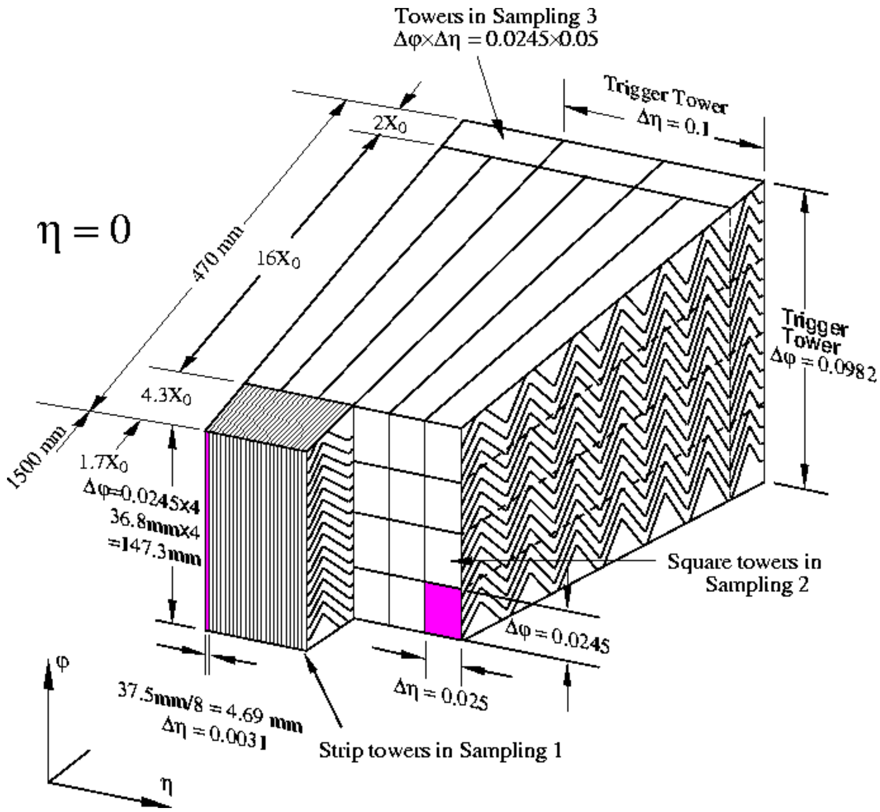

layers with liquid argon (active detection material) and lead (absorber) to induce electromagnetic showers. The LAr EM calorimeters are each more than 20 radiation lengths deep, which provides the high stopping power necessary to properly measure the electromagnetic showers.

The barrel component of the LAr EM calorimeter extends from the center of the detector out to $|\eta| < 1.475$. The calorimeter has a presampler, which measures the energy of any EM shower induced before the calorimeter. This has segmentation of $\Delta\eta = 0.025, \Delta\phi = .01$ There are three "standard" layers in the barrel, which have decreasing segmentation into calorimeter *cells* as one travels radially outward from the interaction point. The first layer has segmentation of $\Delta\eta = 0.003, \Delta\phi = .1$, and is quite thin relative to the other layers at only 4 radiation lengths deep. It provides precise η and ϕ measurements for incoming EM objects. The second layer is the deepest at 16 radiation lengths, with a segmentation of $\Delta\eta = 0.025, \Delta\phi = 0.025$. It

Figure 5.9: A schematic of Tile hadronic calorimeter

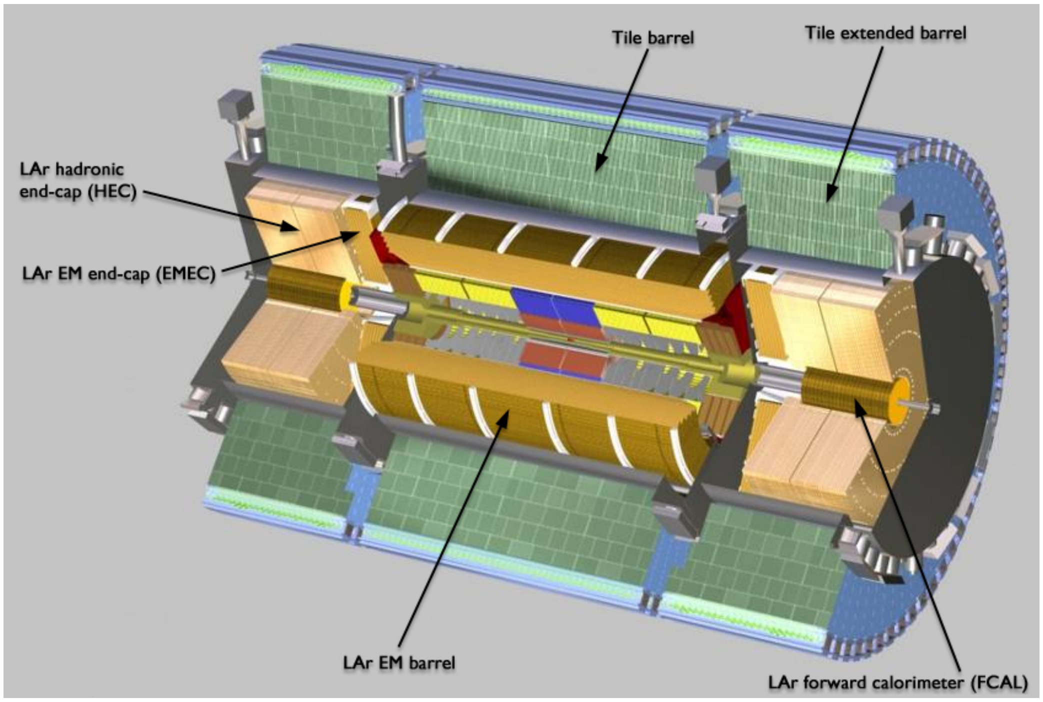

is primarily responsible for stopping the incoming EM particles, which dictates its large relative thickness, and measures most of the energy of the incoming particles. The third layer is only 2 radiation lengths deep, with a rough segmentation of $\Delta\eta = 0.05, \Delta\phi = .025$. The deposition in this layer is primarily used to distinguish hadrons interacting electromagnetically and entering the hadronic calorimeter from the strictly EM objects which are stopped in the second layer.

The barrel EM calorimeter has a similar overall structure, but extends from $1.4 < |\eta| < 3.2$. The segmentation in η is better in the endcap than the barrel; the ϕ segmentation is the same. In total, the EM calorimeters contain about 190000 individual calorimeter cells.

Hadronic Calorimeters

The hadronic calorimetry of ATLAS sits directly outside the EM calorimetry. It contains three subdetectors : the barrel Tile calorimeter, the endcap LAr calorimeter, and the Forward LAr Calorimeter. Similar to the EM calorimeters, these are sampling calorimeters that alternate steel (dense material) with an active layer (plastic scintillator).

The barrel Tile calorimeter extends out to $|\eta| < 1.7$. There are again three layers, which combined give about 10 interactions length of distance, which provides excellent stopping power for hadrons. This is critical to avoid excess *punchthrough* to the muon spectrometer beyond the hadronic calorimeters. The first layer has a depth of 1.5 interaction lengths. The second layer is again the thickest at a depth of 4.1 interaction lengths; most of the energy of incoming particle is deposited here. Both the first and second layer have segmentation of about $\Delta\eta = 0.1, \Delta\phi = 0.1$. Generally, one does not need as fine of granularity in the hadronic calorimeter, since the energy depositions in the hadronic calorimeters will be summed into the composite objects we know as jets. The third layer has a thickness of 1.8 interaction lengths, with a segmentation of $\Delta\eta = 0.2, \Delta\phi = 0.1$. The use of multiple layers allows one to understand the induced hadronic shower as it propagates through the detector material.

The endcap LAr hadronic calorimeter covers the region $1.5 < |\eta| < 3.2$. It is again a sampling calorimeter; the active material is LAr with a copper absorbed. It does not use the accordion shape of the other calorimeters; it has a "standard" flat shape perpendicular to the interaction point. The segmentation varies with η. For $1.5 < |\eta| < 2.5$, the cells are $\Delta\eta = 0.1, \Delta\phi = 0.1$; in the region $2.5 < |\eta| < 3.2$, the cells are $\Delta\eta = 0.2, \Delta\phi = 0.2$ in size.

The final calorimeter in ATLAS is the forward LAr calorimeter. Of those subdetectors which are used for standard reconstruction techniques, the FCal sits at the most extreme values of $3.1 < |\eta| < 4.9$. The FCal itself is made of three subdetectors; FCal1 is actually an electromagnetic module, while FCal2 and FCal3 are hadronic. The absorber in FCal1 is copper, with a liquid argon active medium. FCal2 and FCal3 also use a liquid argon active medium, with a tungsten absorber.

Figure 5.10: The ATLAS muon spectrometer

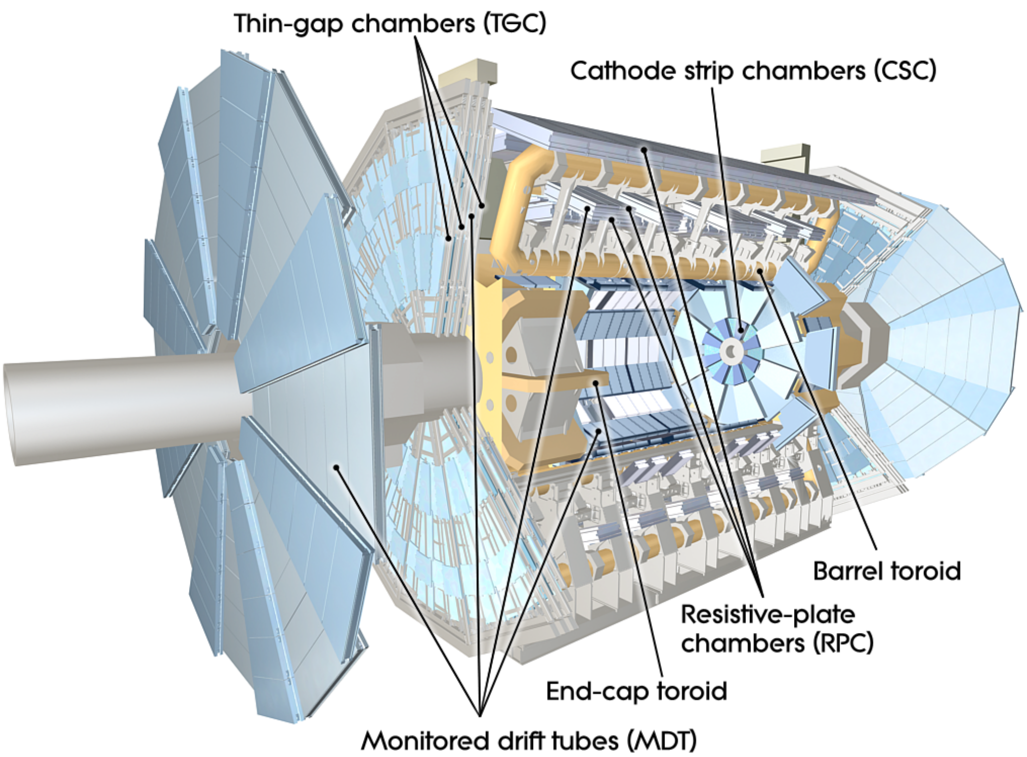

5.4 Muon Spectrometer

The muon spectrometer is the final major subdetector of the ATLAS detector. The muon spectrometer sits outside the hadronic calorimetry, with pseudorapidity coverage out to $|\eta| < 2.7$. The MS is a huge detector, with some detector elements existing as far as 11 m in radius from the interaction point. This system is used almost exclusively to measure the momenta of muons; these are the only measured SM particles which consistently exit the hadronic calorimeters. These systems provide a rough measurement, which is used in triggering (described in Ch.5.5), and a precise measurement to be used in offline event reconstruction as described in Ch.??. The MS produces tracks in a similar way to the ID; the hits in each subdetector are recorded and then tracks are produced from these hits. Muon spectrometer tracks are largely independent of the ID tracks due to the independent solenoidal and toriodal magnet systems used in the ID and MS respectively. The MS consists of four separate

Figure 5.11: A schematic in z/η showing the location of the subdetectors of the muon spectrometer

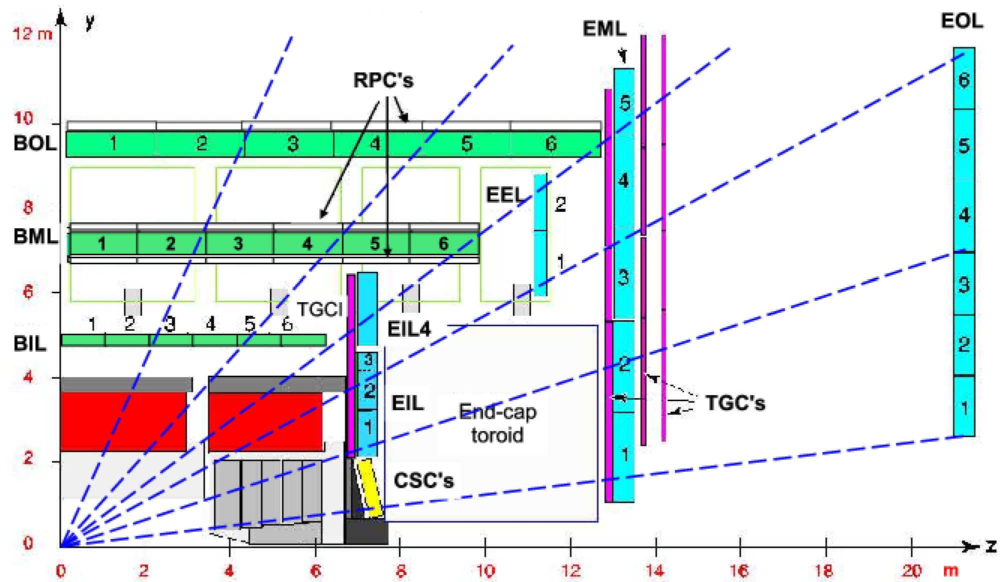

subdetectors: the barrel region is covered by the Resistive Plate Chambers (RPCs) and Monitored Drift Tubes (MDTs) while the endcaps are covered by MDTs, Thin Gap Chambers (TGCs), and Cathode Strip Chambers (CSCs).

Monitored Drift Tubes

The MDT system is the largest individual subdetector of the MS. MDTs provide precision measurements of muon momenta as well as fast measurements used for triggers. There are 1088 MDT chambers providing coverage out to pseudorapidity $|\eta| < 2.7$; each consists of an aluminum tube containing an argon-CO_2 gas mixture. In the center of each tube there 50μm diameter tungsten-rhenium wire at a voltage of 3080 V. A muon entering the tube will induce ionization in the gas, which will "drift" towards the wire due to the voltage. One measures this ionization as a current in the wire; this current comes with a time measurement related to how long it takes the ionization to drift to the wire.

Figure 5.12: Schematic of a Muon Drift Tube chamber

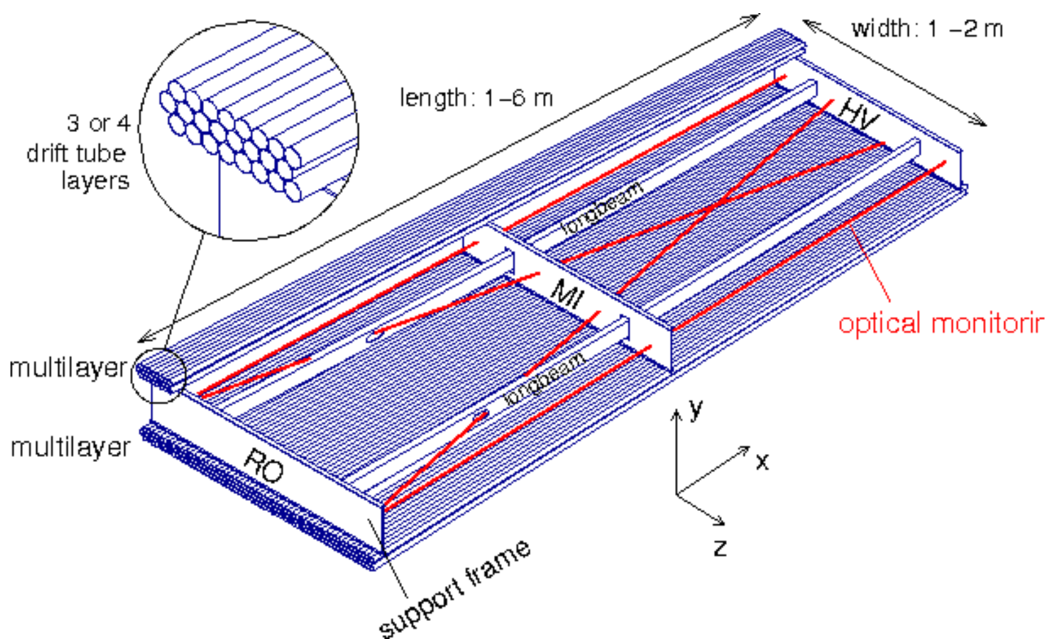

These tubes are layered in a pattern shown in Fig.5.12. Combining the measurements from the tubes in each layer gives good position resolution. The system consists of three subsystems of these layers, at 5 m, 7m, and 9 m from the interaction point. The innermost layer is directly outside the hadronic calorimeter. The combination of these three measurements gives precise momenta measurements for muons.

Resistive Plate Chambers

The RPC system is alternated with the MDT system in the barrel; the first two layers of RPC detectors surround the second MDT layer while the third is outside the final MDT layer. The RPC system covers pseudorapidity $|\eta| < 1.05$. Each RPC consists of two parallel plates at a distance of 2 mm surrounding a $C_2H_2F_4$ mixture. The electric field between these plates is 4.9k kV/mm. Just as in the MDTs, an incoming muon ionizes the gas, and the deposited ionization is collected by the detector (in this case on the plates). It is quite fast, but with a relatively poor spatial resolution of 1 cm. Still, it can provide reasonable ϕ resolution due to its large distance from the interaction point. This is most useful in triggering, where the timing requirements are quite severe. The RPCs are also complement the MDTs by providing a measurement of the non-bending coordinate.

Cathode Strip Chambers

The CSCs are used in place of MDTs in the first layer of the endcaps. This region, at $2.0 < |\eta| < 2.7$, has higher particle multiplicity at the close distance to the interaction point from low-energy photons and neutrons. The MDTs were not equip to deal with the higher particle rate of this region, so the CSCs were designed to deal with this deficiency.

Each CSC consists multiwire proportional chambers, oriented radially outward from the interaction point. These chambers overlap partially in ϕ. The wires contain

Figure 5.13: Photo of the installation of Cathode Strip Chambers and Monitored Drift Tubes

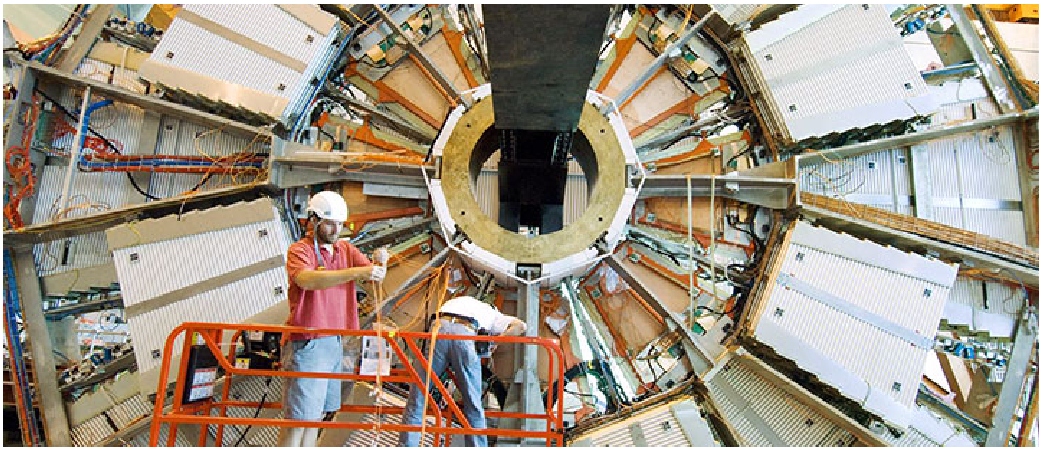

a gas mixture of argon and CO_2, which is ionized when muons enter. The detectors operate with a voltage of 1900 V, with much lower drift times than the MDTs. They provide less hits than MDTs, but their lower drift times lower uptime and reduce the amount of detector overload.

The CSCs are arranged into four planes on the wheels of the muon spectrometer, as seen in Fig.**??**. There are 32 CSCs in total, with 16 on each side of the detector in η.

Thin Gap Chambers

The TGCs serve the purpose of the RPCs in the endcap at pseudorapidity of $1.05 < |\eta| < 2.4$; they provide fast measurements used in triggering. The TGCs are also multiwire proportional chambers a la the CSCs. The fast readouts necessary for trigger are provided by a high electric field and a small wire-to-wire distance of 1.8 mm. These detectors provide both η and ϕ information, allowing the trigger to use as much information as possible when selecting events.

Figure 5.14: Photo of a muon Big Wheel, consisting of Thin Gap Chambers

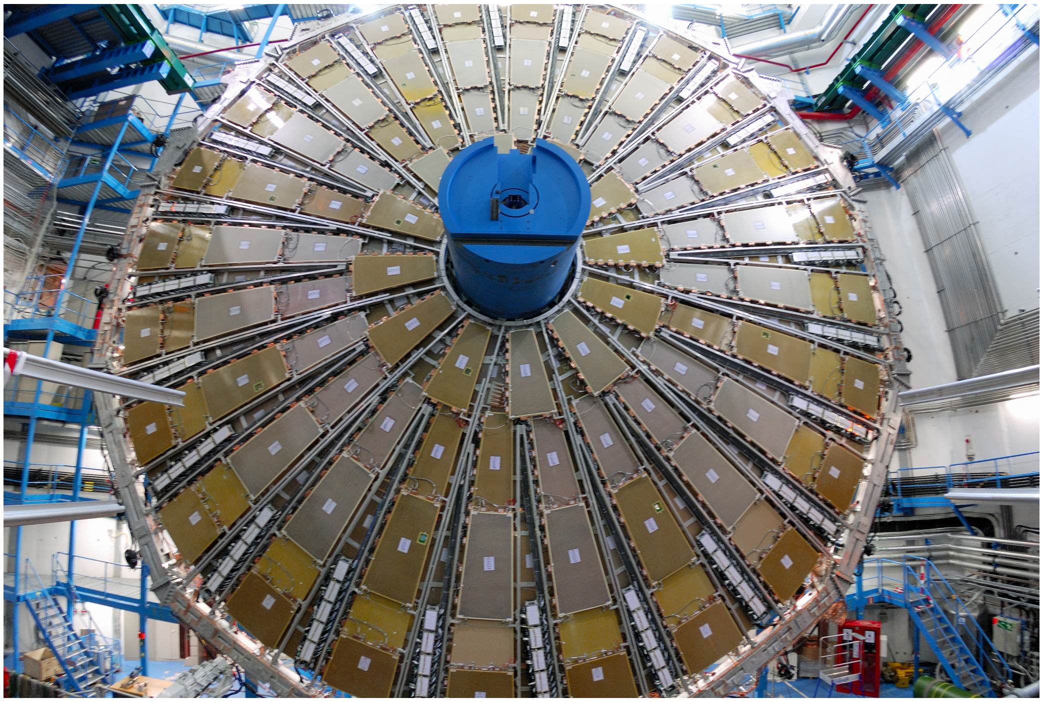

5.5 Trigger System

The data rate delivered by the LHC is staggering [89]. In the 2016 dataset, the collision rate was 40 MHz, meaning a *bunch spacing* of 25 ns. In each of the event, as we saw in Ch.**??**, there are many proton-proton collisions. Most of the collisions are uninteresting, such as elastic scattering of protons, or even inelastic scattering leading to low-energy dijet events. These types of events have been studied in detail in previous experiments.

Even if one is genuinely interested in these events, it's *impossible* to save all of the information available in each event. If all events were written "to tape" (as the jargon goes), ATLAS would store terabytes of data per second. We are limited to only about 1000 Hz readout by computing processing time and storage space. We thus implement a *trigger* which provides fast inspection of events to drastically reduce the data rate from the 40 MHz provided by the LHC to the 1000 Hz we can write to tape for further analysis.

The ATLAS trigger system consists of a two-level trigger, known as the Level-1 trigger (L1 trigger) and the High-Level Trigger (HLT)[4]. Trigger selections are organized into *trigger chains*, where events passing a particular L1 trigger are passed to a corresponding HLT trigger. For example, one would require a particular high-p_{T} muon at L1, with additional quality requirements at HLT. One can also use HLT triggers as prerequisites for each other, as is done in some triggers requiring both jets and $E_{\mathrm{T}}^{\mathrm{miss}}$.

Level-1 Trigger

The L1 trigger is hardware-based, and provides the very fast rejection needed to quickly select events of interest. The L1 trigger uses only what is known as *prompt* data to quickly identify interesting events. Only the calorimeters and the triggering detectors (RPCs and TGCs) of the MS are fast enough to be considered at L1, since the tracking reconstruction algorithms used by the ID and the more precise MS detectors are very slow. This allows quick identification of events with the most interesting physical objects : large missing transverse momentum and high-p_{T} electrons, muons, and jets.

L1 trigger processing is done locally. This means that events are selected without considering the entire available event. Energy deposits over some threshold are reconstructed as *regions of interest*. These RoIs are then compared using pattern recognition hardware to "expected" patterns for the given RoIs. Events with RoIs matching these expected patterns are then handed to the HLT through the Central Trigger Processor. This step alone lowers the data rate down by about three orders of magnitude.

[4]In Run1, ATLAS ran with a three-level trigger system. The L1 was essentially as today; the HLT consisted of two separate systems known as the L2 trigger and the Event Filter (EF). This was changed to the simpler system used today during the shutdown between Run1 and Run2.

High-Level Trigger

The HLT performs the next step, taking the incoming data rate from the L1 trigger of ∼75 kHz down to the ∼1 kHz that can be written to tape. The HLT really performs much like a simplified offline reconstruction, using many common quality and analysis cuts to eliminate uninteresting events. This is done by using computing farms located close to the detector, which process events in parallel. Individually, each event which enters the computing farms takes about 4 seconds to reconstruct; the HLT reconstruction time also has a long tail, which necessitates careful monotoring of the HLT to ensure smooth operation.

HLT triggers are targetted to a particular physics process, such as a $E_{\mathrm{T}}^{\mathrm{miss}}$ trigger, single muon trigger, or multijet trigger. The collection of all triggers is known as the trigger *menu*. Since many low-energy particles are produced in collisions, it is necessary to set a *trigger threshold* on the object of interest; this is really just a fancy naming for a trigger p_{T} cut. Due to the changing luminosity conditions of the LHC, these thresholds change constantly, mostly by increasing thresholds with increasing instaneous luminosity. This allows an approximately constant number of events to be written for further analysis. Triggers which have rates higher than those designated by the menu are *prescaled*. This means writing only some fraction of the triggered events. Of course, for physics analyses, one wishes to investigate all data events passing some set of analysis cuts, so often one uses the "lowest threshold unprescaled trigger". *Turn-on curves* allow one to select the needed offline analysis cut to ensure the trigger is fully efficient. An example turn-on curve for the $E_{\mathrm{T}}^{\mathrm{miss}}$ triggers used in the signal region of this analysis is shown in **??**.

The full set of the lowest threshold unprescaled triggers considered here can be found in Table 5.1. These are the lowest unprescaled triggers associated to the SUSY signal models and Standard Model backgrounds considered in this thesis. More information can be found in [89].

Table 5.1: High-Level Triggers used in this thesis. Descriptions of loose, medium, tight, and isolated can be found in [89]. The d_0 cut refers to a quality cut on the vertex position; this was removed from many triggers in 2016 to increase sensitivity to displaced vertex signals. For most triggers, the increased thresholds in 2016 compared to 2016 were designed to keep the rate approximately equal. The exception is the E_T^{miss} triggers; see 5.5.

Physics Object	Trigger	p_T Threshold (GeV)	Level-1 Seed	Additional Requirements	Approximate Rate (Hz)
2015 Data					
E_T^{miss}	HLT_xe70	70	L1_XE50	-	60
Muon	HLT_mu24_iloose_L1MU15	24	L1_MU15	isolated, loose	130
Muon	HLT_mu50	50	L1_MU15	-	30
Electron	HLT_e24_lhmedium_iloose_L1EM20VH	24	L1_EM20VH	medium OR isolated, loose	140
Electron	HLT_e60_lhmedium	60	L1_EM20VH	medium	10
Electron	HLT_e120_lhloose	120	L1_EM20VH	loose	<10
Photon	HLT_g120_loose	120	L1_EM20VH	loose	20
2016 Data					
E_T^{miss}	HLT_xe100_mht_L1XE50	100	L1_XE50	-	180
Muon	HLT_mu24_ivarmedium	24	L1_MU20	medium	120
Muon	HLT_mu50	50	L1_MU20	-	40
Electron	HLT_e24_lhtight_nod0_ivarloose	24	L1_EM22VHI	tight with no d_0 or loose	110
Electron	HLT_e60_lhmedium_nod0	60	L1_EM22VHI	medium with no d_0	10
Electron	HLT_e140_lhloose_nod0	140	L1_EM22VHI	loose with no d_0	<10
Photon	HLT_g140_loose	140	L1_EM22VHI	loose	20

Razor Triggers

For the analysis presented in this thesis, the *razor triggers* were developed. These are topological triggers, combining both jet and $E_{\mathrm{T}}^{\mathrm{miss}}$ information to select interesting events. In particular, they use the razor variable M_{Δ}^{R}which will be described in Chapter **??**.

Based on 2015 run conditions, these triggers would have allowed the use of a lower offline $E_{\mathrm{T}}^{\mathrm{miss}}$ cut with a similar rate to the nominal $E_{\mathrm{T}}^{\mathrm{miss}}$ triggers. This can be seen in the turn-on curves shown in Figure 5.15. The razor triggers are fully efficient at nearly 100 GeVlower than the corresponding $E_{\mathrm{T}}^{\mathrm{miss}}$ triggers in M_{Δ}^{R}.

There was a quite big change in the 2016 menu, which increased the rate given to $E_{\mathrm{T}}^{\mathrm{miss}}$ triggers drastically. This can be seen in the difference in rate shown between $E_{\mathrm{T}}^{\mathrm{miss}}$ triggers in 2015 and 2016 in Table 5.1. This allowed the $E_{\mathrm{T}}^{\mathrm{miss}}$ triggers to maintain a lower threshold throughout the dataset used in this thesis.

Figure 5.15: Turn-on curves for the razor triggers and nominal $E_{\mathrm{T}}^{\mathrm{miss}}$ trigger. The razor triggers show a much sharper turn-on in M_{Δ}^{R}relative to the $E_{\mathrm{T}}^{\mathrm{miss}}$ trigger. The converse is true for the $E_{\mathrm{T}}^{\mathrm{miss}}$ triggers.

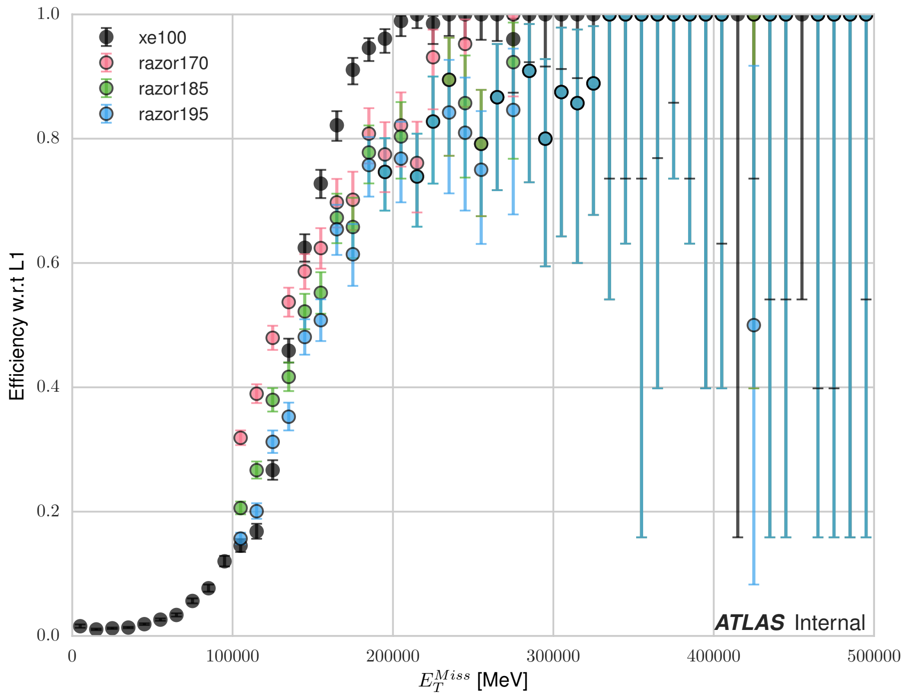

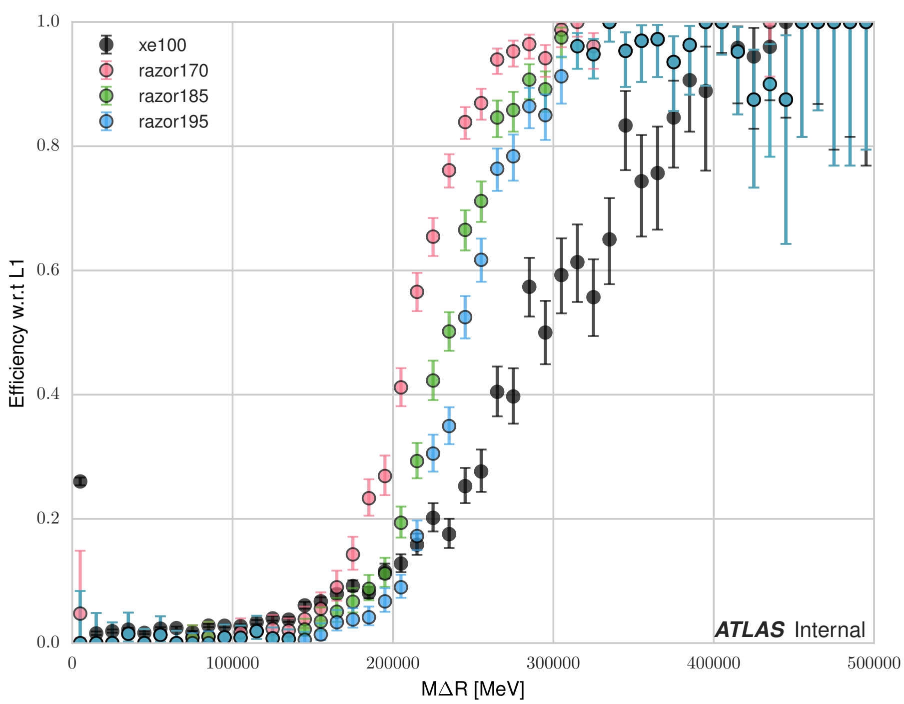

Chapter 6

Event Reconstruction

This chapter describes the reconstruction algorithms used within ATLAS. We will make the distinction between the "primitive" objects which are reconstructed from the detector signals from the "composite" physics objects we use in measurements and searches for new physics.

cite fermilab lectures

6.1 Primitive Object Reconstruction

The primitive objects reconstructed by ATLAS are *tracks* and (calorimeter) *clusters*. These are reconstructed directly from tracking hits and calorimeter energy deposits into cells. Tracks can be further divided into inner detector and muon spectrometer tracks. Calorimeter clusters can be divided into sliding-window clusters and topological clusters (topoclusters).

Inner Detector Tracks

cite paper/note

Inner detector tracks are reconstructed from hits in the inner detector. These hits indicate that a charged particle has passed through the detector material. Due to the 2 T solenoid in the inner detector, the hits associated with any individual particle will be curved; this allows one to measure the momentum of the particle. In any given event, there is upwards of , making it impossible to do any sort of combinatorics to reconstruct tracks[1]. There are two algorithms used by ATLAS track reconstruction,

number

Figure 6.1: The parameters associated to a track.

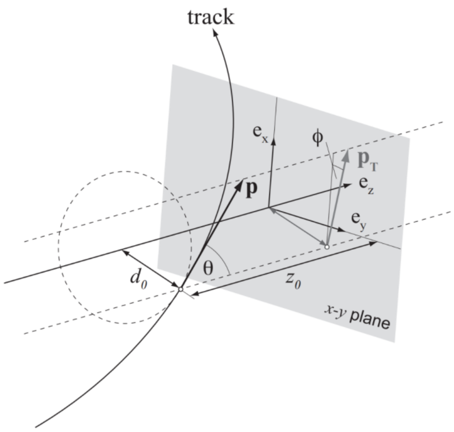

known as *inside-out* and *outside-in*.

ATLAS first employs the inside-out algorithm. First, one assumes the track begins at the interaction point. Moving out from the interaction point, one creates track seeds. Track seeds are proto-tracks constructed from three hits; these hits can be distributed as three pixel hits, two pixel hits and one SCT hit, or three SCT hits. One extrapolates the track and uses a combinatorial Kalman filter , which adds the rest of the pixel and SCT hits to the seeds. This is done seed by seed, so it avoids the combinatorial complexity involved with checking all hits with all seeds. At this point, the algorithm applies an additional filter to avoid ambiguities from nearby tracks. The TRT hits are then added to the seeds in the same procedure; in this way, all hits are associated to a track.

The next step is to figure out the correct kinematics of the track. This is done by applying a fitting algorithm which outputs the best-fit track parameters by minimizing the track distance from hits, weighted by each hit's resolution. These parameters are $(d_0, z_0, \eta, \phi, q/p)$ where d_0 (z_0) is the transverse (longitudinal) impact parameter and q/p is the charge over the track momenta. This set of parameters uniquely defines the trajectory of the charged particle associated to the track; an illustration of a track with these parameters is shown in Fig.6.1.

The other track reconstruction algorithm is the outside-in algorithm. As the name implies, in this case, we start from the outside of the inner detector, in the TRT, and extend the tracks in. One begins by seeding from TRT hits, and extending the track back towards the center of the detector. The same fitting procedure is used as in the inside-out algorithm to find the optimal track parameters. This algorithm is particularly important for finding tracks which originate from interactions with the detector material, especially the SCT. For tracks from primary vertices, this often finds the same tracks as the inside-out algorithm, providing an important check on the consistency of the tracking procedure.

In the high lumonosity environment of the LHC, even the tracks reconstructed from precision detectors such as those of ATLAS inner detector can sometimes lead to fake tracks from simple combinatoric chance. Several quality checks are imposed after track fitting which reduce this background. Seven silicon (pixel + SCT) hits are required for all tracks. No more than two holes are allowed in the pixel detector; holes are expected measurements from the track that are missing in the pixel detector. Finally, tracks with poor fit quality, as measured by χ^2/ndf, are also rejected. Due to the high quality of the silicon measurements in the pixel detector and SCT, these requirements give good track reconstruction efficiency, as seen in Fig.6.2 for simulated events[**ATL-COM-PHYS-2012-1541**].

Sliding-window clusters

The sliding-window algorithm is a way to combine calorimeter cells into composite objects (clusters) to be used as inputs for other algorithms[90]. Sliding-window clusters are the primary inputs to electron and photon reconstruction, as described below. As described in Ch.**??**, the electromagnetic calorimeter has high granularity, with a cell size of $(\eta, \phi) = (.025, .025)$ in the coarsest second layer throughout most of the calorimeter. The "window" consists of 3 by 5 cells in the (η, ϕ) space; all

Figure 6.2: Track reconstruction efficiency as a function of track p_{T} and η. The efficiency is defined as the number of reconstructed tracks divided by the number of generate charged particles.

(a) Track reconstruction as a function of p_{T}. (b) Track reconstruction as a function of η.

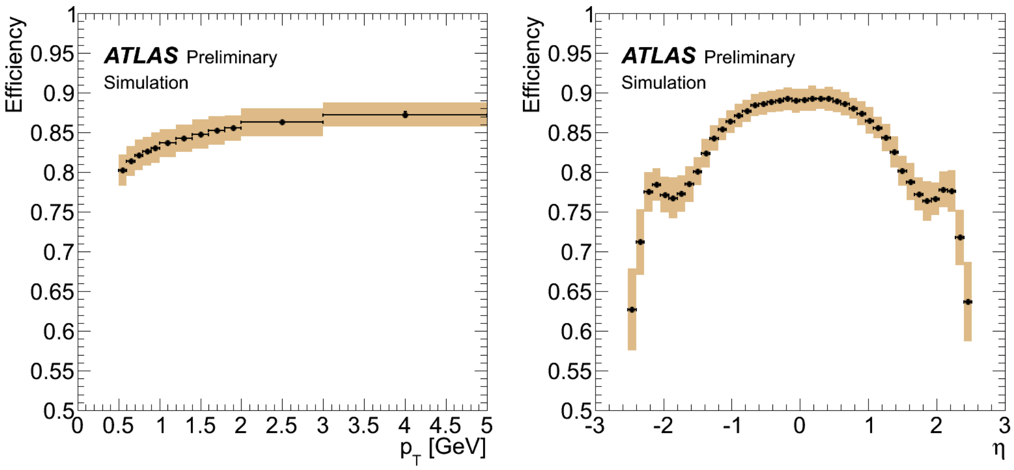

layers are added on this same 2D space. One translates this window over the space and seeds a cluster whenever the energy sum of the cells is maximized. If the seed energy is greater than 2.5 GeV, this seed is called a sliding-window cluster. This choice was motivated to optimize the reconstruction efficiency of proto-electrons and proto-photons while rejecting fakes from electronic noise and additional particles from pileup vertices.

Topological clusters

cite paper/note

Topoclusters are the output of the algorithm used within ATLAS to combine hadronic and electromagnetic calorimeter cells in a way which extracts signal from a background of significant electronic noise[91]. They are the primary input to the algorithms which reconstruct jets.

Topological clusters are reconstructed from calorimeter cells in the following way. First, one maps all cells onto a single $\eta - \phi$ plane so one can speak of *neighboring* cells. Two cells are considered neighboring if they are in the same layer and directly adjacent, or if they are in adjacent layers and overlap in $\eta - \phi$ space. The *significance* ξ_{cell} of a cell during a given event is

$$\xi_{\text{cell}} = \frac{E_{\text{cell}}}{\sigma_{\text{noise,cell}}} \tag{6.1}$$

where $\sigma_{\text{noise,cell}}$ is measured for each cell in ATLAS and E_{cell} measures the current energy level of the cell. One thinks of this as the measurement of the energy *over threshold* for the cell.

Topocluster *seeds* are defined as calorimeter cells which have a significance $\xi_{\text{cell}} > 4$. These are the inputs to the algorithm; one iteratively tests all cells adjacent to these seeds for $\xi_{\text{cell}} > 2$. Each cells passing this selection is then added to the topocluster, and the procedure is repeated. When the algorithm reaches the point where there are no additional adjacent cells with $\xi_{\text{cell}} > 2$, every positive-energy cell adjacent to the current proto-cluster is added. This collection of cells is summed; the summed object is known as a topocluster. An example of this procedure for a simulation dijet event is shown in Fig.6.3.

Muon Spectrometer Tracks

6.2 Physics Object Reconstruction

There are essentially sixe objects used in ATLAS searches for new physics: electrons, photons, muons, τ-jets, jets, and $E_{\text{T}}^{\text{miss}}$. The reconstruction of these objects is described here. A very convenient summary plot is shown in Fig.6.4. In this thesis, we present a search for new physics in a zero lepton final state; we will provide additional details about jet and $E_{\text{T}}^{\text{miss}}$ reconstruction.

Figure 6.3: Example of topoclustering on a simulated dijet event.

(a) All cells with $\xi_{\mathrm{cell}} > 4$.

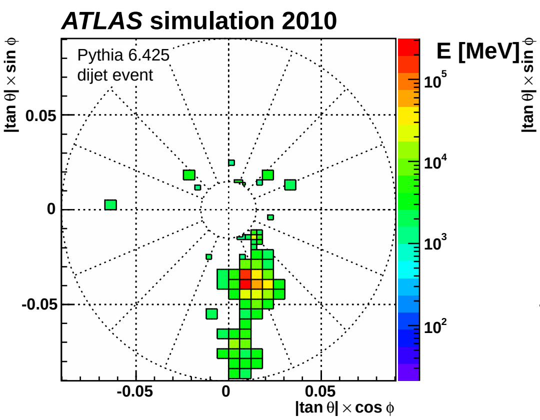

(b) All cells with $\xi_{\mathrm{cell}} > 2$.

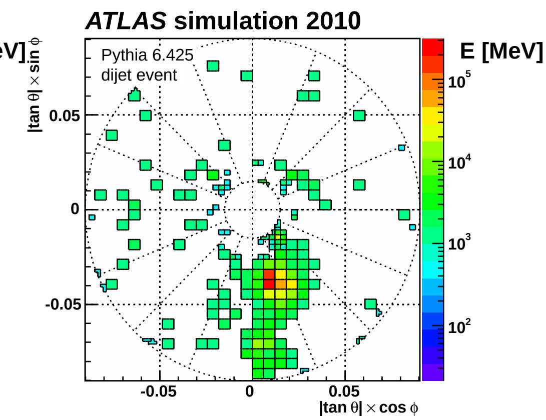

(c) All clustered cells.

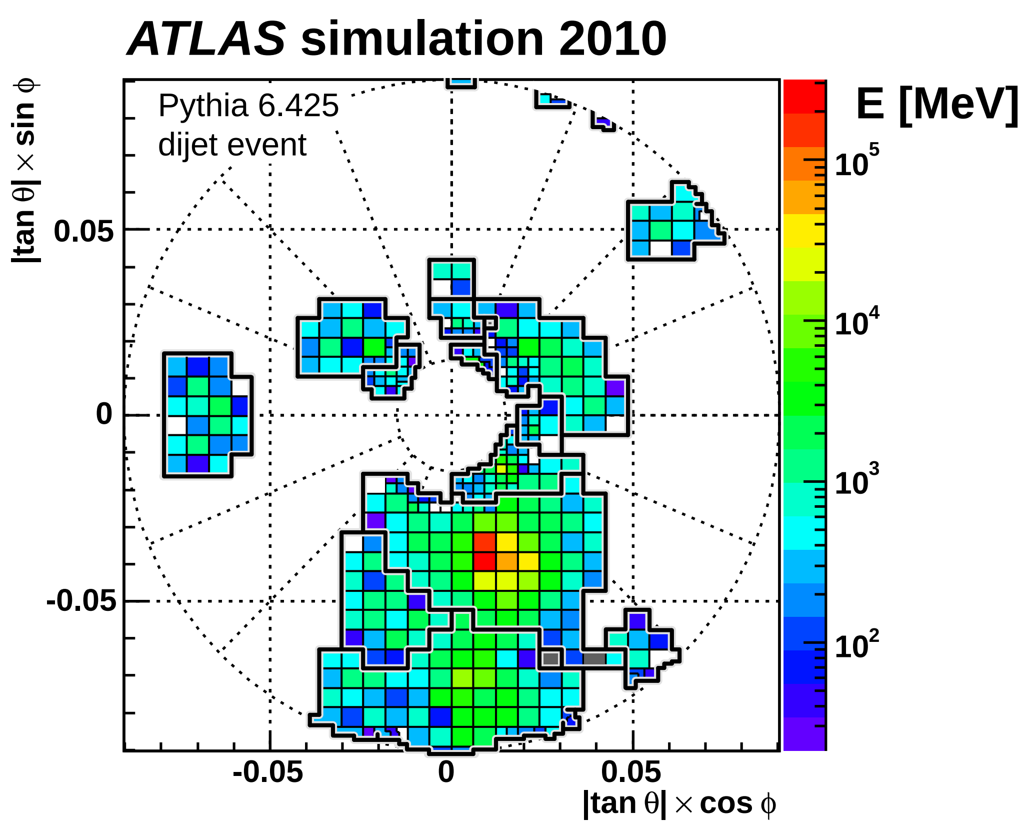

Figure 6.4: Graphic showing the interactions of reconstructed objects with the ATLAS detector. Solid lines indicate the particle is interacting with the detector, while dashed lines show those which are ignored.

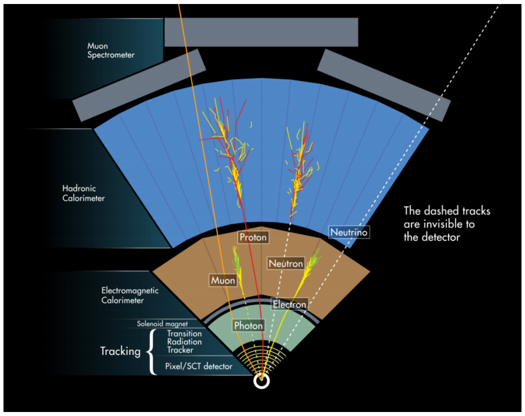

Electrons

Electrons are reconstructed by associating electromagnetic showers in the EM calorimeter with charged particle tracks left in the ID[90]. The electromagnetic clusters are reconstructed

Photons

cite paper/note

Muons

cite paper/note

Jets

cite paper/note

Missing Transverse Momentum

cite paper/notes

6.3 Maybe PFlow?

Chapter 7

The Recursive Jigsaw Technique

Here you can write some introductory remarks about your chapter. I like to give each sentence its own line.

When you need a new paragraph, just skip an extra line.

7.1 Razor variables

By using the asterisk to start a new section, I keep the section from appearing in the table of contents. If you want your sections to be numbered and to appear in the table of contents, remove the asterisk.

7.2 SuperRazor variables

7.3 The Recursive Jigsaw Technique

7.4 Variables used in the search for zero lepton SUSY

Chapter 8

Title of Chapter 1

Chapter 9

Title of Chapter 1

Here you can write some introductory remarks about your chapter. I like to give each sentence its own line.

When you need a new paragraph, just skip an extra line.

9.1 Object reconstruction

Photons, Muons, and Electrons

Jets

Missing transverse momentum

Probably longer, show some plots from the PUB note that we worked on

9.2 Signal regions

Gluino signal regions

Squark signal regions

Compressed signal regions

9.3 Background estimation

Z vv

W ev

ttbar

Chapter 10

Title of Chapter 1

Here you can write some introductory remarks about your chapter. I like to give each sentence its own line.

When you need a new paragraph, just skip an extra line.

10.1 Statistical Analysis

maybe to be moved to an appendix

10.2 Signal Region distributions

10.3 Pull Plots

10.4 Systematic Uncertainties

10.5 Exclusion plots

Conclusion

Here you can write some introductory remarks about your chapter. I like to give each sentence its own line.

When you need a new paragraph, just skip an extra line.

10.6 New Section

By using the asterisk to start a new section, I keep the section from appearing in the table of contents. If you want your sections to be numbered and to appear in the table of contents, remove the asterisk.

Bibliography

[1] O. Perdereau, *Planck 2015 cosmological results*, AIP Conf. Proc. **1743** (2016) p. 050014.

[2] N. Aghanim et al., *Planck 2016 intermediate results. LI. Features in the cosmic microwave background temperature power spectrum and shifts in cosmological parameters* (2016), arXiv: 1608.02487 [astro-ph.CO].

[3] J. S. Schwinger, *On Quantum electrodynamics and the magnetic moment of the electron*, Phys. Rev. **73** (1948) p. 416.

[4] S. Laporta and E. Remiddi, *The Analytical value of the electron (g-2) at order alpha**3 in QED*, Phys. Lett. **B379** (1996) p. 283, arXiv: hep-ph/9602417 [hep-ph].

[5] S. Schael et al., *Precision electroweak measurements on the Z resonance*, Phys. Rept. **427** (2006) p. 257, arXiv: hep-ex/0509008 [hep-ex].

[6] S. L. Glashow, *Partial Symmetries of Weak Interactions*, Nucl. Phys. **22** (1961) p. 579.

[7] S. Weinberg, *A Model of Leptons*, Phys. Rev. Lett. **19** (1967) p. 1264.

[8] A. Salam, *Weak and Electromagnetic Interactions*, Conf. Proc. **C680519** (1968) p. 367.

[9] M. Gell-Mann, *A Schematic Model of Baryons and Mesons*, Phys. Lett. **8** (1964) p. 214.

[10] G. Zweig, "An SU(3) model for strong interaction symmetry and its breaking. Version 2," *DEVELOPMENTS IN THE QUARK THEORY OF HADRONS. VOL. 1. 1964 - 1978*, ed. by D. Lichtenberg and S. P. Rosen, 1964 p. 22, URL: http://inspirehep.net/record/4674/files/cern-th-412.pdf.

[11] S. Weinberg, *Implications of Dynamical Symmetry Breaking*, Phys. Rev. **D13** (1976) p. 974.

[12] S. Weinberg, *Implications of Dynamical Symmetry Breaking: An Addendum*, Phys. Rev. **D19** (1979) p. 1277.

[13] E. Gildener, *Gauge Symmetry Hierarchies*, Phys. Rev. **D14** (1976) p. 1667.

[14] L. Susskind, *Dynamics of Spontaneous Symmetry Breaking in the Weinberg-Salam Theory*, Phys. Rev. **D20** (1979) p. 2619.

[15] S. P. Martin, "A Supersymmetry Primer," 1997, eprint: `arXiv:hep-ph/9709356`.

[16] V. C. Rubin and W. K. Ford Jr., *Rotation of the Andromeda Nebula from a Spectroscopic Survey of Emission Regions*, Astrophys. J. **159** (1970) p. 379.

[17] M. S. Roberts and R. N. Whitehurst, *"The rotation curve and geometry of M31 at large galactocentric distances*, Astrophys. J. **201** (1970) p. 327.

[18] V. C. Rubin, N. Thonnard, and W. K. Ford Jr., *Rotational properties of 21 SC galaxies with a large range of luminosities and radii, from NGC 4605 /R = 4kpc/ to UGC 2885 /R = 122 kpc/*, Astrophys. J. **238** (1980) p. 471.

[19] V. C. Rubin et al., *Rotation velocities of 16 SA galaxies and a comparison of Sa, Sb, and SC rotation properties*, Astrophys. J. **289** (1985) p. 81.

[20] A. Bosma, *21-cm line studies of spiral galaxies. 2. The distribution and kinematics of neutral hydrogen in spiral galaxies of various morphological types.*, Astron. J. **86** (1981) p. 1825.

[21] M. Persic, P. Salucci, and F. Stel, *The Universal rotation curve of spiral galaxies: 1. The Dark matter connection*, Mon. Not. Roy. Astron. Soc. **281** (1996) p. 27, arXiv: `astro-ph/9506004 [astro-ph]`.

[22] M. Lisanti, "Lectures on Dark Matter Physics," 2016, eprint: `arXiv:1603.03797`.

[23] H. Miyazawa, *Baryon Number Changing Currents*, Prog. Theor. Phys. **36** (1966) p. 1266.

[24] J.-L. Gervais and B. Sakita, *Generalizations of dual models*, Nucl. Phys. **B34** (1971) p. 477.

[25] J.-L. Gervais and B. Sakita, *Field Theory Interpretation of Supergauges in Dual Models*, Nucl. Phys. **B34** (1971) p. 632.

[26] Yu. A. Golfand and E. P. Likhtman, *Extension of the Algebra of Poincare Group Generators and Violation of p Invariance*, JETP Lett. **13** (1971) p. 323, [Pisma Zh. Eksp. Teor. Fiz.13,452(1971)].

[27] A. Neveu and J. H. Schwarz, *Factorizable dual model of pions*, Nucl. Phys. **B31** (1971) p. 86.

[28] A. Neveu and J. H. Schwarz, *Quark Model of Dual Pions*, Phys. Rev. **D4** (1971) p. 1109.

[29] D. V. Volkov and V. P. Akulov, *Is the Neutrino a Goldstone Particle?* Phys. Lett. **B46** (1973) p. 109.

[30] J. Wess and B. Zumino, *A Lagrangian Model Invariant Under Supergauge Transformations*, Phys. Lett. **B49** (1974) p. 52.

[31] A. Salam and J. A. Strathdee, *Supersymmetry and Nonabelian Gauges*, Phys. Lett. **B51** (1974) p. 353.

[32] S. Ferrara, J. Wess, and B. Zumino, *Supergauge Multiplets and Superfields*, Phys. Lett. **B51** (1974) p. 239.

[33] J. Wess and B. Zumino, *Supergauge Transformations in Four-Dimensions*, Nucl. Phys. **B70** (1974) p. 39.

[34] J. D. Lykken, "Introduction to supersymmetry," *Fields, strings and duality. Proceedings, Summer School, Theoretical Advanced Study Institute in Elementary Particle Physics, TASI'96, Boulder, USA, June 2-28, 1996*, 1996 p. 85, arXiv: `hep-th/9612114 [hep-th]`, URL: `http://lss.fnal.gov/cgi-bin/find_paper.pl?pub-96-445-T`.

[35] A. Kobakhidze, "Intro to SUSY," 2016, URL: `https://indico.cern.ch/event/443176/page/5225-pre-susy-programme`.

[36] G. R. Farrar and P. Fayet, *Phenomenology of the Production, Decay, and Detection of New Hadronic States Associated with Supersymmetry*, Phys. Lett. **B76** (1978) p. 575.

[37] ATLAS Collaboration, *Search for the electroweak production of supersymmetric particles in $\sqrt{s} = 8$ TeV pp collisions with the ATLAS detector*, Phys. Rev. D **93** (2016) p. 052002, arXiv: 1509.07152 [hep-ex].

[38] ATLAS Collaboration, *Summary of the searches for squarks and gluinos using $\sqrt{s} = 8$ TeV pp collisions with the ATLAS experiment at the LHC*, JHEP **10** (2015) p. 054, arXiv: 1507.05525 [hep-ex].

[39] ATLAS Collaboration, *ATLAS Run 1 searches for direct pair production of third-generation squarks at the Large Hadron Collider*, Eur. Phys. J. C **75** (2015) p. 510, arXiv: 1506.08616 [hep-ex].

[40] CMS Collaboration, *Search for supersymmetry with razor variables in pp collisions at $\sqrt{s} = 7$ TeV*, Phys. Rev. D **90** (2014) p. 112001, arXiv: 1405.3961 [hep-ex].

[41] CMS Collaboration, *Inclusive search for supersymmetry using razor variables in pp collisions at $\sqrt{s} = 7$ TeV*, Phys. Rev. Lett. **111** (2013) p. 081802, arXiv: 1212.6961 [hep-ex].

[42] CMS Collaboration, *Search for Supersymmetry in pp Collisions at 7 TeV in Events with Jets and Missing Transverse Energy*, Phys. Lett. B **698** (2011) p. 196, arXiv: 1101.1628 [hep-ex].

[43] CMS Collaboration, *Search for Supersymmetry at the LHC in Events with Jets and Missing Transverse Energy*, Phys. Rev. Lett. **107** (2011) p. 221804, arXiv: 1109.2352 [hep-ex].

[44] CMS Collaboration, *Search for supersymmetry in hadronic final states using M_{T2} in pp collisions at $\sqrt{s} = 7$ TeV*, JHEP **10** (2012) p. 018, arXiv: 1207.1798 [hep-ex].

[45] CMS Collaboration, *Searches for supersymmetry using the M_{T2} variable in hadronic events produced in pp collisions at 8 TeV*, JHEP **05** (2015) p. 078, arXiv: 1502.04358 [hep-ex].

[46] CMS Collaboration, *Search for new physics with the M_{T2} variable in all-jets final states produced in pp collisions at $\sqrt{s} = 13$ TeV* (2016), arXiv: 1603.04053 [hep-ex].

[47] ATLAS Collaboration, *Multi-channel search for squarks and gluinos in $\sqrt{s} = 7$ TeV pp collisions with the ATLAS detector at the LHC*, Eur. Phys. J. C **73** (2013) p. 2362, arXiv: 1212.6149 [hep-ex].

[48] Y. Grossman, “Introduction to the SM,” 2016, URL: https://indico.fnal.gov/sessionDisplay.py?sessionId=3&confId=11505#20160811.

[49] ().

[50] P. W. Higgs, *Broken Symmetries and the Masses of Gauge Bosons*, Phys. Rev. Lett. **13** (1964) p. 508.

[51] ATLAS Collaboration, *Observation of a new particle in the search for the Standard Model Higgs boson with the ATLAS detector at the LHC*, Phys. Lett. B **716** (2012) p. 1, arXiv: 1207.7214 [hep-ex].

[52] CMS Collaboration, *Observation of a new boson at a mass of 125 GeV with the CMS experiment at the LHC*, Phys. Lett. B **716** (2012) p. 30, arXiv: 1207.7235 [hep-ex].

[53] A. Chodos et al., *A New Extended Model of Hadrons*, Phys. Rev. **D9** (1974) p. 3471.

[54] A. Chodos et al., *Baryon Structure in the Bag Theory*, Phys. Rev. **D10** (1974) p. 2599.

[55] J. C. Collins, D. E. Soper, and G. F. Sterman, *Factorization of Hard Processes in QCD*, Adv. Ser. Direct. High Energy Phys. **5** (1989) p. 1, arXiv: hep-ph/0409313 [hep-ph].

[56] K. A. Olive et al., *Review of Particle Physics*, Chin. Phys. **C38** (2014) p. 090001.

[57] N. Cabibbo, *Unitary Symmetry and Leptonic Decays*, Phys. Rev. Lett. **10** (1963) p. 531, [,648(1963)].

[58] M. Kobayashi and T. Maskawa, *CP Violation in the Renormalizable Theory of Weak Interaction*, Prog. Theor. Phys. **49** (1973) p. 652.

[59] W. F. L. Hollik, *Radiative Corrections in the Standard Model and their Role for Precision Tests of the Electroweak Theory*, Fortsch. Phys. **38** (1990) p. 165.

[60] D. Yu. Bardin et al., *ELECTROWEAK RADIATIVE CORRECTIONS TO DEEP INELASTIC SCATTERING AT HERA! CHARGED CURRENT SCATTERING*, Z. Phys. **C44** (1989) p. 149.

[61] D. C. Kennedy et al., *Electroweak Cross-Sections and Asymmetries at the Z0*, Nucl. Phys. **B321** (1989) p. 83.

[62] A. Sirlin, *Radiative Corrections in the SU(2)-L x U(1) Theory: A Simple Renormalization Framework*, Phys. Rev. **D22** (1980) p. 971.

[63] S. Fanchiotti, B. A. Kniehl, and A. Sirlin, *Incorporation of QCD effects in basic corrections of the electroweak theory*, Phys. Rev. **D48** (1993) p. 307, arXiv: `hep-ph/9212285 [hep-ph]`.

[64] C. Quigg, "Cosmic Neutrinos," *Proceedings, 35th SLAC Summer Institute on Particle Physics: Dark matter: From the cosmos to the Laboratory (SSI 2007): Menlo Park, California, July 30- August 10, 2007*, 2008, arXiv: `0802.0013 [hep-ph]`, URL: `http://lss.fnal.gov/cgi-bin/find_paper.pl?conf-07-417`.

[65] S. R. Coleman and J. Mandula, *All Possible Symmetries of the S Matrix*, Phys. Rev. **159** (1967) p. 1251.

[66] R. Haag, J. T. Lopuszanski, and M. Sohnius, *All Possible Generators of Supersymmetries of the s Matrix*, Nucl. Phys. **B88** (1975) p. 257.

[67] A. Salam and J. A. Strathdee, *On Superfields and Fermi-Bose Symmetry*, Phys. Rev. **D11** (1975) p. 1521.

[68] S. Dimopoulos and H. Georgi, *Softly Broken Supersymmetry and SU(5)*, Nucl. Phys. **B193** (1981) p. 150.

[69] S. Dimopoulos, S. Raby, and F. Wilczek, *Supersymmetry and the Scale of Unification*, Phys. Rev. **D24** (1981) p. 1681.

[70] L. E. Ibanez and G. G. Ross, *Low-Energy Predictions in Supersymmetric Grand Unified Theories*, Phys. Lett. **B105** (1981) p. 439.

[71] W. J. Marciano and G. Senjanovic, *Predictions of Supersymmetric Grand Unified Theories*, Phys. Rev. **D25** (1982) p. 3092.

[72] L. Girardello and M. T. Grisaru, *Soft Breaking of Supersymmetry*, Nucl. Phys. **B194** (1982) p. 65.

[73] D. J. H. Chung et al., *The Soft supersymmetry breaking Lagrangian: Theory and applications*, Phys. Rept. **407** (2005) p. 1, arXiv: hep-ph/0312378 [hep-ph].

[74] J. Hisano et al., *Lepton flavor violation in the supersymmetric standard model with seesaw induced neutrino masses*, Phys. Lett. **B357** (1995) p. 579, arXiv: hep-ph/9501407 [hep-ph].

[75] F. Gabbiani et al., *A Complete analysis of FCNC and CP constraints in general SUSY extensions of the standard model*, Nucl. Phys. **B477** (1996) p. 321, arXiv: hep-ph/9604387 [hep-ph].

[76] F. Gabbiani and A. Masiero, *FCNC in Generalized Supersymmetric Theories*, Nucl. Phys. **B322** (1989) p. 235.

[77] J. S. Hagelin, S. Kelley, and T. Tanaka, *Supersymmetric flavor changing neutral currents: Exact amplitudes and phenomenological analysis*, Nucl. Phys. **B415** (1994) p. 293.

[78] J. S. Hagelin, S. Kelley, and V. Ziegler, *Using gauge coupling unification and proton decay to test minimal supersymmetric SU(5)*, Phys. Lett. **B342** (1995) p. 145, arXiv: hep-ph/9406366 [hep-ph].

[79] D. Choudhury et al., *Constraints on nonuniversal soft terms from flavor changing neutral currents*, Phys. Lett. **B342** (1995) p. 180, arXiv: hep-ph/9408275 [hep-ph].

[80] R. Barbieri and L. J. Hall, *Signals for supersymmetric unification*, Phys. Lett. **B338** (1994) p. 212, arXiv: hep-ph/9408406 [hep-ph].

[81] B. de Carlos, J. A. Casas, and J. M. Moreno, *Constraints on supersymmetric theories from mu —¿ e gamma*, Phys. Rev. **D53** (1996) p. 6398, arXiv: hep-ph/9507377 [hep-ph].

[82] J. A. Casas and S. Dimopoulos, *Stability bounds on flavor violating trilinear soft terms in the MSSM*, Phys. Lett. **B387** (1996) p. 107, arXiv: hep-ph/9606237 [hep-ph].

[83] C. Borschensky et al., *Squark and gluino production cross sections in pp collisions at $\sqrt{s}$ = 13, 14, 33 and 100 TeV*, Eur. Phys. J. **C74** (2014) p. 3174, arXiv: 1407.5066 [hep-ph].

[84] M. Klasen, M. Pohl, and G. Sigl, *Indirect and direct search for dark matter*, Prog. Part. Nucl. Phys. **85** (2015) p. 1, arXiv: 1507.03800 [hep-ph].

[85] L. Evans and P. Bryant, *LHC Machine*, JINST **3** (2008) S08001.

[86] V. Shiltsev, "Accelerator Physics and Technology," 2016, URL: https://indico.fnal.gov/sessionDisplay.py?sessionId=3&confId=11505#20160811.

[87] *LEP design report*, Copies shelved as reports in LEP, PS and SPS libraries, Geneva: CERN, 1984, URL: https://cds.cern.ch/record/102083.

[88] ATLAS Collaboration, *The ATLAS Experiment at the CERN Large Hadron Collider*, JINST **3** (2008) S08003.

[89] ATLAS Collaboration, *2015 start-up trigger menu and initial performance assessment of the ATLAS trigger using Run-2 data*, ATL-DAQ-PUB-2016-001, 2016, URL: https://cds.cern.ch/record/2136007/.

[90] ATLAS Collaboration, *Electron reconstruction and identification efficiency measurements with the ATLAS detector using the 2011 LHC proton–proton collision data*, Eur. Phys. J. C **74** (2014) p. 2941, arXiv: 1404.2240 [hep-ex].

[91] ATLAS Collaboration, *Topological cell clustering in the ATLAS calorimeters and its performance in LHC Run 1* (2016), arXiv: 1603.02934 [hep-ex].

The Standard Model

In this appendix, we provide a brief overview of the basic ingredients involved in construction of the Standard Model Lagrangian : quantum field theory, symmetries, and symmetry breaking.

Quantum Field Theory

cite Yuval's lectures and notes somehow

In this section, we provide a brief overview of the necessary concepts from Quantum Field Theory (QFT).

In modern physics, the laws of nature are described by the "action" S, with the imposition of the principle of minimum action. The action is the integral over the spacetime coordinates of the "Lagrangian density" $\mathcal{L}$, or Lagrangian for short. The Lagrangian is a function of "fields"; general fields will be called $\phi(x^\mu)$, where the indices μ run over the space-time coordinates. We can then write the action S as

cite

$$S = \int d^4x \mathcal{L}[\phi_i(x^\mu), \partial_\mu \phi_i(x^\mu)] \tag{10.1}$$

where we have an additional summation over i (of the different fields). Generally, we impose the following constraints on the Lagrangian :

1. Translational invariance - The Lagrangian is only a function of the fields ϕ and their derivatives $\partial_\mu \phi$
2. Locality - The Lagrangian is only a function of one point x_μ in spacetime.

3. Reality condition - The Lagrangian is real to conserve probability.

4. Lorentz invariance - The Lagrangian is invariant under the Poincarégroup of spacetime.

5. Analyticity - The Lagrangian is an analytical function of the fields; this is to allow the use of pertubation theory.

6. Invariance and Naturalness - The Lagrangian is invariant under some internal symmetry groups; in fact, the Lagrangian will have *all* terms allowed by the imposed symmetry groups.

maybe add in ref here

7. Renormalizabilty - The Lagrangian will be renormalizable - in practice, this means there will not be terms with more than power 4 in the fields.

The key item from the point of view of this thesis is that of "Invariance and Natural". We impose a set of "symmetries" and then our Lagragian is the most general which is allowed by those symmetries.

Symmetries

Symmetries can be seen as the fundamental guiding concept of modern physics. Symmetries are described by "groups". . To illustrate the importance of symmetries and their mathematical description, groups, we start here with two of the simplest and most useful examples : $\mathbb{Z}_2$and $U(1)$.

cite?

$\mathbb{Z}_2$symmetry

$\mathbb{Z}_2$symmetry is the simplest example of a "discrete" symmetry. Consider the most general Lagrangian of a single real scalar field $\phi(x_\mu)$

$$\mathcal{L}_\phi = \frac{1}{2}\partial_\mu\phi\partial^\mu\phi - \frac{m^2}{2}\phi^2 - \frac{\mu}{2\sqrt{2}}\phi^3 - \lambda\phi^4 \tag{10.2}$$

Now we *impose* the symmetry

$$\mathcal{L}(\phi) = \mathcal{L}(-\phi) \tag{10.3}$$

This has the effect of restricting the allowed terms of the Lagrangian. In particular, we can see the term $\phi^3 \to -\phi^3$ under the symmetry transformation, and thus must be disallowed by this symmetry. This means under the imposition of this particular symmetry, our Lagrangian should be rewritten as

$$\mathcal{L}_\phi = \frac{1}{2}\partial_\mu\phi\partial^\mu\phi - \frac{m^2}{2}\phi^2 - \lambda\phi^4 \tag{10.4}$$

The effect of this symmetry is that the total number of ϕ particles can only change by even numbers, since the only interaction term $\lambda\phi^4$ is an even power of the field. This symmetry is often imposed in supersymmetric theories, as we will see in Chapter 3.

$U(1)$ symmetry

$U(1)$ is the simplest example of a continuous (or *Lie*) group. Now consider a theory with a single complex scalar field $\phi = \operatorname{Re}\phi + i\operatorname{Im}\phi$

$$\mathcal{L}_\phi = \delta_{i,j}\frac{1}{2}\partial_\mu\phi_i\partial^\mu\phi_j - \frac{m^2}{2}\phi_i\phi_j - \frac{\mu}{2\sqrt{2}}\phi_i\phi_j\phi_k - \lambda\phi_i\phi_j\phi_k\phi_l \tag{10.5}$$

where $i, j, k, l = Re, Im$. In this case, we impose the following $U(1)$ symmetry : $\phi \to e^{i\theta}, \phi^* \to e^{-i\theta}$. We see immediately that this again disallows the third-order terms, and we can write a theory of a complex scalar field with $U(1)$ symmetry as

$$\mathcal{L}_\phi = \partial_\mu\phi\partial^\mu\phi^* - \frac{m^2}{2}\phi\phi^* - -\lambda(\phi\phi^*)^2 \tag{10.6}$$

Local symmetries

The two examples considered above are "global" symmetries in the sense that the symmetry transformation does not depends on the spacetime coordinate x_μ. We know look at local symmetries; in this case, for example with a local $U(1)$ symmetry, the transformation has the form $\phi(x_\mu) \to e^{i\theta(x_m u)}\phi(x_\mu)$. These symmetries are also known as "gauge" symmetries; all symmetries of the Standard Model are gauge symmetries.

There are wide-ranging consequences to the imposition of local symmetries. To begin, we note that the derivative terms of the Lagrangian 10.2 are *not* invariant under a local symmetry transformation

$$\partial_\mu\phi(x_\mu) \to \partial_\mu(e^(i\theta(x_\mu)\phi(x_\mu)) = (1 + i\theta(x_\mu))e^(i\theta(x_\mu)\phi(x_\mu) \tag{10.7}$$

GET THIS RIGHT

This leads us to note that the kinetic terms of the Lagrangian are also not invariant under a gauge symmetry. This would lead to a model with no dynamics, which is clearly unsatisfactory.

Let us take inspiration from the case of global symmetries. We need to define a so-called "covariant" derivative D^μ such that

$$D^\mu\phi \to e^{iq\theta(x^\mu)D^\mu\phi} \tag{10.8}$$

$$D^\mu\phi^* \to e^{-iq\theta(x^\mu)D^\mu\phi} \tag{10.9}$$

$$\tag{10.10}$$

Since ϕ andϕ^* transforms with the opposite phase, this will lead the invariance of the Lagrangian under our local gauge transformation. This D^μ is of the following form

$$D^\mu = \partial_\mu - igqA^\mu \tag{10.11}$$

where A^μ is a vector field we introduce with the transformation law

$$A^\mu \to A^\mu - \frac{1}{g}\partial_\mu \theta \tag{10.12}$$

and g is the coupling constant associated to vector field. This vector field A^μ is also known as a "gauge" field.

Since we need to add all allowed terms to the Lagrangian, we define

$$F^{\mu\nu} = A^\mu A^\nu - A^\nu A^\mu \tag{10.13}$$

and then we must also add the kinetic term :

$$\mathcal{L}_{\text{gauge}} = -\frac{1}{4}F^{\mu\nu}F_{\mu\nu} \tag{10.14}$$

The most general renormalizable Lagrangian with fermion and scalar fields can be written in the following form

$$\mathcal{L} = \mathcal{L}_{kin} + \mathcal{L}_\phi + \mathcal{L}_\psi + \mathcal{L}Yukawa \tag{10.15}$$

Symmetry breaking and the Higgs mechanism

Here we view some examples of symmetry breaking. We investigate breaking of a global $U(1)$ symmetry and a local $U(1)$ symmetry. The SM will break the electroweak symmetry $SU(2)xU(1)$, and in Chapter 3 we will see how supersymmetry must also be broken.

There are two ideas of symmetry breaking

- Explicit symmetry breaking by a small parameter - in this case, we have a small parameter which breaks an "approximate" symmetry of our Lagrangian. An example would be the theory of the single scalar field 10.2, when $\mu << m^2$ and

$\mu << \lambda$. In this case, we can often ignore the small term when considering low-energy processes.

- Spontaneous symmetry breaking (SSB) - spontaneous symmetry breaking occurs when the Lagrangian is symmetric with respect to a given symmetry transformation, but the ground state of the theory is *not* symmetric with respect to that transformation. This can have some fascintating consequences, as we will see in the following examples

Symmetry breaking a

U(1) global symmetry breaking

Consider the theory of a complex scalar field under the $U(1)$ symmetry, or the transformation

$$\phi \to e^{i\theta}\phi \tag{10.16}$$

The Lagrangian for this theory is

$$\mathcal{L} = \partial^\mu \phi^\dagger \partial_\mu \phi + \frac{\mu^2}{2}\phi^\dagger \phi + \frac{\lambda}{4}(\phi^\dagger \phi)^2 \tag{10.17}$$

Let us write this theory in terms of two scalar fields, h and ξ : $\phi = (h + i\xi)/\sqrt(2)$. The Lagrangian can then be written as

$$\mathcal{L} = \partial^\mu h \partial_\mu h + \partial^\mu \xi dmu \xi - \frac{\mu^2}{2}(h^2 + \xi^2) - \frac{\lambda}{4}(h^2 + \xi^2)^2 \tag{10.18}$$

First, note that the theory is only stable when $\lambda > 0$. To understand the effect of SSB, we now enforce that $\mu^2 < 0$, and define $v^2 = -\mu^2/\lambda$. We can then write the scalar potential of this theory as :

$$V(\phi) = \lambda(\phi^\dagger \phi - v^2/2)^2 \tag{10.19}$$

Minimizing this equation with respect to ϕ, we can see that the "vacuum expectation value" of the theory is

$$2 < \phi^\dagger \phi > = < h^2 + \xi^2 > = v^2 \tag{10.20}$$

We now reach the "breaking" point of this procedure. In the (h, ξ) plane, the minima form a circle of radius v. We are free to choose any of these minima to expand our Lagrangian around; the physics is not affected by this choice. For convenience, choose $< h >= v, < \xi^2 >= 0$.

Now, let us define $h' = h - v, \xi' = \xi$ with VEVs $< h' >= 0, < \xi' >= 0$. We can then write our spontaneously broken Lagrangian in the form

$$\mathcal{L} = \frac{1}{2}\partial_\mu h' \partial^\mu h' + \frac{1}{2}\partial_\mu \xi' \partial^\mu \xi' - \lambda v^2 h'^2 - \lambda v h'(h'^2 + \xi'^2) - \lambda(h'^2 + \xi'^2)^2 \qquad (10.21)$$